Lehrstuhl für Computergestützte Modellierung und Simulation
TUM School of Engineering and Design
Technical University of Munich

Partial lumping for isogeometric finite cell analysis with approximate dual functions

Scientific work to obtain the degree

Bachelor of Science (B.Sc.)

at the TUM School of Engineering and Design
of the Technical University of Munich.

Supervised by Prof. Dr.-Ing. André Borrmann
Tim Bürchner, M.Sc.
Lehrstuhl für Computergestützte Modellierung und Simulation

Submitted by Julius Leo Weidinger ([redacted])
[redacted]
[redacted] [redacted]
e-Mail: [redacted]

Submitted on 16. April 2024

Abstract

The Isogeometric Finite Cell Analysis (IGA-FCM) is a combination of the Isogeometric Analysis (IGA) and the Finite Cell Method (FCM) that can be applied to solve immersed problems. IGA is a well-established higher-order Finite Element Method (FEM) that relies on B-splines basis functions, as ansatz and test functions, and is known for its high accuracy per Degree of Freedom (dof). FCM is a fictitious domain method that simplifies the cumbersome mesh generation for geometrical complex structures.
In this thesis, IGA-FCM is applied to solve a one-dimensional wave propagation problem. Efficient solvers for such a problem depend upon diagonal system matrices for the explicit time marching scheme. For IGA, dual basis functions or approximate dual basis functions with mass lumping, as test functions, can attain such matrices for boundary-conforming problems without compromising accuracy. Herein, those are applied for the discretization of the immersed wave problem. Their asymptotic and transient accuracy is quantified and compared against regular IGA-FCM with B-spline test functions and no mass lumping.

Zusammenfassung

Die Isogeometrische Finite-Zellen-Analyse (IGA-FCM) ist eine Kombination aus der Isogeometrischen Analyse (IGA) und der Finite-Zellen-Methode (FCM), die zur Lösung eingebetteter Probleme eingesetzt werden kann. IGA ist eine etablierte Finite-Elemente-Methode FEM höherer Ordnung, die auf B-Spline Basisfunktionen als Ansatz- und Testfunktionen beruht und für ihre hohe Genauigkeit pro Freiheitsgrad (dof) bekannt ist. FCM ist eine Fictitious Domain Methode, die die mühsame Netzgenerierung für geometrisch komplexe Strukturen vereinfacht.
In dieser Arbeit wird IGA-FCM zur Lösung eines eindimensionalen Wellenausbreitungsproblems angewandt. Effiziente Löser für ein solches Problem basieren auf diagonalen Systemmatrizen für das explizite Zeitmarschverfahren. Für IGA können duale Basisfunktionen oder approximierte duale Basisfunktionen mit Massenlumping als Testfunktionen solche Matrizen für randkonforme Probleme erzeugenn, ohne die Genauigkeit zu beeinträchtigen. In dieser Abschlussarbeit werden diese für die Diskretisierung des eingebetteten Wellenausbreitungsproblems angewandt. Ihre asymptotische und transiente Genauigkeit wird quantifiziert und mit regulärem IGA-FCM mit B-Spline Testfunktionen und ohne Massenlumping verglichen.

Contents

List of Figures

List of Tables

Acronyms

CAD	Computer Aided Design
CDM	Central Difference Method
dof	Degree of Freedom
FCM	Finite Cell Method
FEA	Finite Element Analysis
FEM	Finite Element Method
FWI	Full Waveform Inversion
GL	Gauss-Legendre
IGA	Isogeometric Analysis
IGA-FCM	Isogeometric Finite Cell Analysis
IMEX	Implicit-Explicit
NDT	Non-Destructive Testing
NURBS	Non-Uniform Rational B-Splines
PDE	Partial Differential Equation
SCM	Spectral Cell Method

Chapter 1

Introduction

1.1 Motivation and Application

Tom Hughes et al. have introduced the Isogeometric Analysis (IGA) in 2004 [1]. The initial motivation was to merge Computer Aided Design (CAD) with the Finite Element Analysis (FEA), to cut the time and cost of the transition process for the model between the two. CAD software products predominantly use Non-Uniform Rational B-Splines (NURBS) [2] in order to represent any curves, surfaces, or three-dimensional shapes accurately [3]. The fundamental idea of Hughes et al. for IGA was to use these NURBS as basis functions for the analysis, see [1].

Despite the original objective, also other methods of geometrical descriptions were established in IGA within the last 20 years, e.g., T-splines [4], U-splines [5] or S-splines [6]. Furthermore, other frames of application for IGA are continuously identified because IGA has, as a higher-order Finite Element Method (FEM), high convergence rates and a high accuracy per Degree of Freedom (dof) [1][7]. One of them is the Full Waveform Inversion (FWI) based on a combination of IGA and FCM [8]. The FCM allows the generation of a simple mesh for structures with complex geometries by adding a fictitious domain [9].

The FWI is a computational method that uses measured wave signals to reconstruct material models [10]. It originated from seismic tomography [11] and is nowadays also utilized for biomedical applications [12][13] and Non-Destructive Testing (NDT) [14][15], to find enclosed fractures and voids. The efficiency and accuracy of the FWI largely depend on the properties of its wave field solver. Efficient solvers combine diagonal system matrices with an explicit time integration [16]. Diagonal system matrices attain their structures when inverted and yield smaller maximum eigenvalues. Hence, a greater critical time step applies for the explicit time integration, and less memory capacity is required.

The results presented by Bürchner et al. in [8] for consistent IGA-FCM as a wave field solver for an immersed setting show high convergence rates and good accuracy. Due to the nature of the B-spline basis functions used for IGA-FCM, the system matrices are not diagonal. When mass lumping is applied, the p-convergence and the corresponding accuracy are lost.

1.2 Goal of this thesis

Approaches with the Petrov-Galerkin Method, using dual and approximate dual basis functions as test functions, for IGA were already studied in [17][18][19][20][21]. It was shown for boundary conforming problems, that dual basis functions yield diagonal mass matrices due to its bi-orthogonality and that row-summing can be applied for approximate dual basis functions, without compromising their accuracy.

This thesis aims to investigate the accuracy of Petrov-Galerkin approaches, with dual and approximate dual basis functions as test functions, for IGA-FCM when applied to an one-dimensional immersed problem. Similar to the work describe in Section 1.1 by Bürchner et al. in [8], a one dimensional elastic wave is discretized and an explicit time integration scheme is deployed.

1.3 Overview

In Chapter 2 all essential mathematical definitions and computational methods applied in this thesis are introduced. Beginning with the definition of the Partial Differential Equation (PDE) of the one-dimensional elastic wave equation. Secondly, the underlying mathematics of IGA are presented, focusing on constructing B-splines basis functions and discretizing the elastic wave equation. The following summarizes the important properties of dual functionals and all computational steps required to construct dual and approximate dual basis functions. Fourth, FCM is introduced and explained how its discretization of immersed problems works. At the end of this chapter, row-summing is elaborated as the mass lumping technique of choice in this work.

In the following part, Chapter 3, IGA-FCM is used to discretize the propagation of the one-dimensional elastic wave. Initially, the parameters of the non-boundary conforming problem are set and all combination of mass lumping, ansatz functions and basis functions for IGA-FCM are specified. Then, the two errors that quantify the asymptotic accuracy are computed and the results are visualized. Thirdly, the initial and boundary conditions for the elastic wave propagation are defined and the Central Difference Method (CDM) is demonstrated. Afterwards, an appropriate measure for the transient accuracy is identified and calculated. As a wrap up, all the results obtained for the asymptotic and transient accuracy of the different versions of IGA-FCM are compared and discussed.

At the end in Chapter 4, the findings of this work are summarized and an outlook is given for potential future research. An Implicit-Explicit (IMEX) approach for the lumped IGA-FCM with approximate dual basis functions seems promising.

Chapter 2

Theory

2.1 1D elastic wave equation

The one-dimensional wave equation describes the propagation of waves in terms of a displacement field $u \in \mathbb{R}$ in the one-dimensional space $x \in \mathbb{R}$. The mathematical definitions in this section are derived from [22]. Considering the balance of linear momentum, the elastic wave equation for a one-dimensional domain Ω and time frame $t \in [0, T_{\max}]$, is defined by

$$\rho(x)\ddot{u}(x,t) + \frac{\partial}{\partial x}\left(\mu(x)\frac{\partial}{\partial x}u(x,t)\right) = f(x,t), \qquad x \in \Omega, \quad t \in [0, T_{\max}]. \tag{2.1}$$

Here, $\rho(x)$ denotes the density and $\mu(x)$ the shear modulus of the medium. The wave field is expressed by $u(x,t)$ and its acceleration by $\ddot{u}(x,t)$, as the second derivative with respect to time t. Lastly, $f(x,t)$ denotes the external applied force. In addition, initial conditions, for $t = 0$, are introduced for the displacement of the wave field u and its velocity $\dot{u}$, given by

$$u(x,0) = u_0(x), \qquad x \in \Omega, \quad t = 0, \tag{2.2}$$

$$\dot{u}(x,0) = \dot{u}_0(x), \qquad x \in \Omega, \quad t = 0. \tag{2.3}$$

The shear modulus $\mu(x)$ can be replaced in Equation (2.5) by introducing the wave speed

$$c(x) = \sqrt{\frac{\mu(x)}{\rho(x)}}. \tag{2.4}$$

In the context of this thesis, it is assumed that the medium is isotropic and homogeneous, so the material parameters are independent of the space x. Therefore the density and the wave speed are constants, ρ_0 and c_0. The initial conditions remain unchanged and with Equation (2.4) the one-dimensional wave equation is given by

$$\rho_0\ddot{u}(x,t) + \frac{\partial}{\partial x}\left(\rho_0 c_0^2\frac{\partial}{\partial x}u(x,t)\right) = f(x,t), \qquad x \in \Omega, \quad t \in [0, T_{\max}]. \tag{2.5}$$

Equation (2.5) is referred to as the *strong form* of the elastic wave equation [22]. The boundary conditions are specified in the introduction of the problem for the numerical investigation in Chapter 3.

2.2 Isogeometric analysis

To construct B-spline basis functions, a polynomial degree p and a knot vector $\boldsymbol{\Xi}$ must be chosen. The knot vector is a set of one-dimensional coordinates of the parametric space Ω and is written in a non-descending order as $\boldsymbol{\Xi} = \{\xi_1, \xi_2, \ldots, \xi_{n+p+1}\}$. Each knot $\xi_i \in \mathbb{R}$ has an index i, for $i = 1, 2, \ldots, n + p + 1$ and n is the total number of basis functions.

A knot vector can be *uniform*, *non-uniform* or *open* [1]. In a uniform knot vector, all knots are equally spaced. It is also possible that knots are unevenly spaced or that multiple knots lie on the same coordinate, known as repeated knots. Then, the knot vector is referred to as non-uniform. The multiplicity k of a knot indicates how many knots lie on the same coordinate. Only open knot vectors are used in this work. They have a multiplicity of $k = p + 1$ for the knots at each end and $k = 1$ for the knots in between.

B-spline basis functions can be derived using the Cox-de Boor recursive formula [23]. The initial condition starting with piecewise constants for $p = 0$ is

$$N_{i,0}(\xi) = \begin{cases} 1 & \text{if} \quad \xi_i \leq \xi < \xi_{i+1} \\ 0 & \text{otherwise} \end{cases}. \tag{2.6}$$

For higher polynomial orders of $p = 1, 2, \ldots$, the B-splines are defined recursively by

$$N_{i,p}(\xi) = \frac{\xi - \xi_i}{\xi_{i+p} - \xi_i} N_{i,p-1}(\xi) + \frac{\xi_{i+p+1} - \xi}{\xi_{i+p+1} - \xi_{i+1}} N_{i+1,p-1}(\xi). \tag{2.7}$$

The derivatives of the B-spline basis functions with respect to the spatial coordinates can be obtained by applying standard differentiation techniques described in [24]. Within this work, only the first derivative is required, which is given by

$$\frac{d}{d\xi} N_{i,p}(\xi) = \frac{p}{\xi_{i+p} - \xi_i} N_{i,p-1}(\xi) - \frac{p}{\xi_{i+p+1} - \xi_{i+1}} N_{i+1,p-1}(\xi). \tag{2.8}$$

A sample set of B-spline basis functions $\mathbf{N} = \{N_i\}_n$, for $p = 2$ and an open knot vector $\boldsymbol{\Xi} = [0.0, 0.0, 0.0, 0.2, 0.4, 0.6, 0.8, 1.0, 1.0, 1.0]$, can be seen in Figure 2.1.

The B-spline basis functions have a continuity of C^{p-k} across the knot boundaries, where k denotes the multiplicity of the knot. For a detailed explanation of the continuity of B-splines and the advantage of an open knot vector, the reader is referred to [1]. It can also be observed that every basis function $N_{i,p}(\xi)$ is supported on $p + 1$ elements [20]. Analogously, there are $p + 1$ non-zero basis functions in each element.

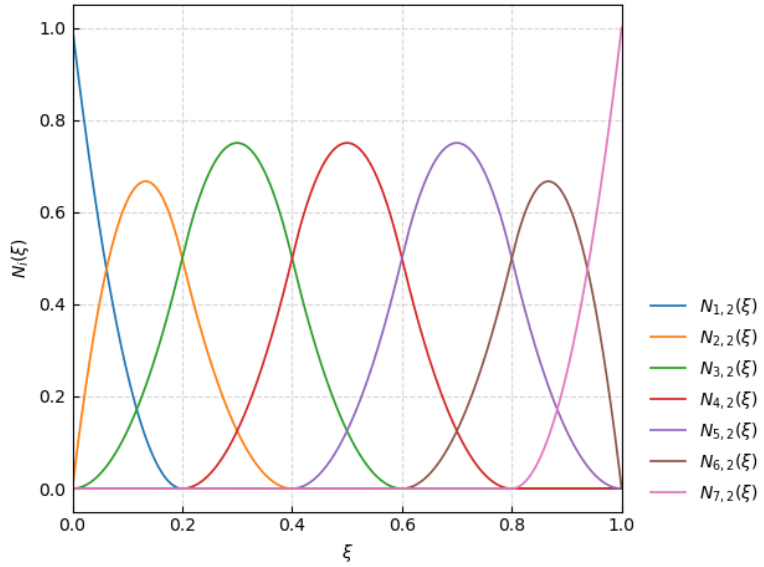

Figure 2.1: Quadratic B-spline basis functions $\mathbf{N}$

For the spatial discretization of the one-dimensional domain Ω, the weak form of the elastic wave equation is required. The derivation follows [24]. The weak form of the elastic wave equation is obtained by multiplying the strong form of the elastic wave equation, Equation (2.5), with a test function $v(x)$, from an appropriate ansatz space V, and integration over the parametric domain Ω.

$$\int_\Omega \rho_0 v(x)\ddot{u}(x,t)\mathrm{d}x - \int_\Omega v(x)\frac{\partial}{\partial x}\left(\rho_0 c_0^2 \frac{\partial}{\partial x}u(x,t)\right)\mathrm{d}x = \int_\Omega v(x)f(x,t)\mathrm{d}x. \tag{2.9}$$

Integration by parts of the second term on the left-hand side of Equation (2.9) is given by

$$\begin{aligned} &-\int_\Omega v(x)\frac{\partial}{\partial x}\left(\rho_0 c_0^2 \frac{\partial}{\partial x}u(x,t)\right)\mathrm{d}x = \\ &\int_\Omega \rho_0 c_0^2 \frac{\partial}{\partial x}v(x)\frac{\partial}{\partial x}u(x,t)\mathrm{d}x - \left[\rho_0 c_0^2 v(x)\frac{\partial}{\partial x}u(x)\right]_{x_{min}}^{x_{max}} \end{aligned} \tag{2.10}$$

and according to [22], for the one-dimensional wave equation, the term $\left[\rho_0 c_0^2 v(x)\frac{\partial}{\partial x}u(x)\right]_{x_{min}}^{x_{max}}$ vanishes for homogeneous Neumann boundary conditions. So, the weak form of the one-dimensional elastic wave equation is defined by

$$\int_\Omega \rho_0 v(x)\ddot{u}(x,t)\mathrm{d}x + \int_\Omega \rho_0 c_0^2 \frac{\partial}{\partial x}v(x)\frac{\partial}{\partial x}u(x,t)\mathrm{d}x = \int_\Omega v(x)f(x,t)\mathrm{d}x. \tag{2.11}$$

To spatially discretize the displacement of the wave field $u(x,t)$ and the test function $v(x)$, they are substituted with an approximate solution [25].

The approximations $\tilde{u}$ and $\tilde{v}$ are a linear combination of basis functions $N_i(x) \in V_\mathrm{h} \subset V$ with their corresponding coefficients $\hat{u}_i(t)$ and $\hat{v}_i$ given by

$$u(x,t) \approx \tilde{u}(x,t) = \sum_{i=1}^{n} N_i(x)\hat{u}_i(t), \tag{2.12}$$

$$v(x) \approx \tilde{v}(x) = \sum_{i=1}^{n} N_i(x)\hat{v}_i. \tag{2.13}$$

The number of basis functions n is equivalent to the total number of dof's and the index $i \in \{1,\dots,n\}$ indicates the i'th dof [26]. For the Bubnov-Galerkin method, the basis functions deployed for the wave field and the test functions are identical. On the downside, other sets of basis functions can be used to approximate the test function $v(x)$, known as the Petrov-Galerkin method [17]. Dual and approximate dual basis functions for B-spline basis functions for the Petrov-Galerkin method are introduced in Subsections 2.3.1 and 2.3.2. With the approximations of the equations above, the weak form of the one-dimensional elastic wave equation is given as

$$\begin{aligned} &\int_\Omega \rho_0 \sum_{i=1}^{n} N_i(x)\hat{v}_i \sum_{j=1}^{n} N_j(x)\ddot{\hat{u}}_j(t)\mathrm{d}x + \\ &\int_\Omega \rho_0 c_0^2 \sum_{i=1}^{n} \frac{\partial}{\partial x}N_i(x)\hat{v}_i \sum_{j=1}^{n} \frac{\partial}{\partial x}N_j(x)\hat{u}_j(t)\mathrm{d}x = \int_\Omega \sum_{i=1}^{n} N_i(x)\hat{v}_i f(x,t)\mathrm{d}x. \end{aligned} \tag{2.14}$$

Since the weak form must hold for any $v \in V_\mathrm{h}$ and thus for all combinations of $\hat{v}_i$ [25], the spatially discretized form of the elastic wave equation can be defined for $i = 1,\dots,n$ by

$$\begin{aligned} &\int_\Omega \rho_0 N_i(x) \sum_{j=1}^{n} N_j(x)\ddot{\hat{u}}_j(t)\mathrm{d}x + \\ &\int_\Omega \rho_0 c_0^2 \frac{\partial}{\partial x}N_i(x) \sum_{j=1}^{n} \frac{\partial}{\partial x}N_j(x)\hat{u}_i(t)\mathrm{d}x = \int_\Omega N_i(x) f(x,t)\mathrm{d}x. \end{aligned} \tag{2.15}$$

Equation (2.15) can also be written in a matrix notation as the space-discrete form of the elastic wave equation given by

$$\mathbf{M}\ddot{\hat{\boldsymbol{u}}}(t) + \mathbf{K}\hat{\boldsymbol{u}}(t) = \hat{\boldsymbol{f}}(t). \tag{2.16}$$

The mass matrix $\mathbf{M}$, the stiffness matrix $\mathbf{K}$ and the external force vector $\hat{\boldsymbol{f}}$ are defined by

$$M_{ij} = \int_\Omega \rho_0 N_i N_j \mathrm{d}x, \tag{2.17}$$

$$K_{ij} = \int_\Omega \rho_0 c_0^2 \frac{\partial}{\partial x}N_i \frac{\partial}{\partial x}N_j \mathrm{d}x, \tag{2.18}$$

$$f_i = \int_\Omega N_i f \mathrm{d}x. \tag{2.19}$$

In this thesis the quantities above are computed on an element basis, analogous to the traditional FEM [24]. The element quantities, denoted with the subscript e, are assembled by the operator A into their global ones, given by

$$\mathbf{M} = \mathsf{A}\mathbf{M}^e \tag{2.20}$$
$$\mathbf{K} = \mathsf{A}\mathbf{K}^e \tag{2.21}$$
$$\boldsymbol{f} = \mathsf{A}\boldsymbol{f}^e \tag{2.22}$$

As the integration is carried out on an element basis, the standardized element coordinates $\xi \in \Omega^e = [-1, 1]$ are used. To map the results back to the global coordinates x, the determinant of the Jacobian $J = \frac{\partial x}{\partial \xi}$ is deployed, and the integrals are therefore given by

$$\mathbf{M}^e = \int_{\Omega^e} \rho_0 \mathbf{N}^T \mathbf{N} det(J) \mathrm{d}\xi, \tag{2.23}$$
$$\mathbf{K}^e = \int_{\Omega^e} \rho_0 c_0^2 \left(\frac{1}{det(J)} \frac{\partial}{\partial \xi} \right) \mathbf{N}^T \left(\frac{1}{det(J)} \frac{\partial}{\partial \xi} \mathbf{N} \right) det(J) \mathrm{d}\xi, \tag{2.24}$$
$$\boldsymbol{f}^e = \int_{\Omega^e} \mathbf{N} f det(J) \mathrm{d}\xi. \tag{2.25}$$

For each differentiation of the basis functions $\mathbf{N}$ with respect to ξ in Equation (2.24), an addition multiplication with $\frac{1}{det(J)}$ is required to attain the correct mapping of the coordinates. All n^e non-zero basis functions within the element are arranged in the vector $\mathbf{N} = [N_1, N_2, \ldots, N_{n^e}]^T$ in the corresponding order to the dof's.

This thesis's integration scheme of choice is the Gauss-Legendre (GL) integration [26]. For an arbitrary function $a(x)$, the integral over an arbitrary interval I is computed by

$$\int_I a(x) \mathrm{d}x = \sum_{i=1}^{n_{int}} w_i a(x_i). \tag{2.26}$$

Hereby denotes n_{int} the total number of integration points and w_i the corresponding integration weights of the GL integration scheme. The number of integration points is set to $n_{int} = p + 1$ for each element for every integration on an element level with a polynomial degree p.

2.3 Dual functionals and dual basis functions

This section specifies the characteristic properties of dual basis functions before dual and approximate dual basis functions for B-spline basis functions are introduced. This section is derived from [19], where Dornisch et al. utilized dual and approximate dual basis functions for B-splines for the isogeometric mortar method.

When N_j is an arbitrary one-dimensional B-spline basis function, with local support on the interval Ω_j. Then the characteristic dual functional f_i is given by

$$f_i(N_j) = \delta_{i,j}. \tag{2.27}$$

Where $\delta_{i,j}$ denotes the Kronecker delta as

$$\delta_{i,j} = \begin{cases} 1 & \text{if} \quad i = j \\ 0 & \text{otherwise} \end{cases}. \tag{2.28}$$

The property of Equation (2.27) is known as bi-orthogonality. The dual functional for a set of n one-dimensional B-spline basis functions $\mathbf{N} = \{N_i\}_n$ and a corresponding set of dual basis functions $\boldsymbol{\lambda} = \{\lambda_i\}_n$, both defined on the interval Ω, is given by

$$f_i(N_j) = \int_{\Omega_j} N_j \lambda_i \mathrm{d}x. \tag{2.29}$$

Combining Equations (2.27) and (2.29) derives the duality relation

$$\int_{\Omega_j} N_j \lambda_i \mathrm{d}x = \delta_{i,j}. \tag{2.30}$$

For the context of this thesis, the mathematical definitions given above are adequate. More detailed definitions and proofs for dual functionals and dual basis functions can be found in [27] [28].

Another important aspect of dual basis functions is the degree of polynomial reproduction. For $r = 0, \ldots, p$, a polynomial function x^r can be reproduced by

$$x^r = \sum_{j=1}^{n} c_j^r \lambda_j \qquad \text{with} \qquad c_j^r = \int_{\Omega} x^r N_j \mathrm{d}s. \tag{2.31}$$

Dual basis functions only fulfill the property of Equation (2.31) if their linear span contains all polynomials of $\leq p$, according to [29].

2.3.1 Dual basis functions

Dual basis functions for B-spline basis functions can be obtained with the inversion of the Gram matrix. Hence, they are also denoted as inverse gramian dual basis functions. The computational steps required for their construction are summarized in this section and are derived from [19] [20].

Starting with the computation of the Gram matrix $\mathbf{G}_{\mathrm{N,N}}$, as the integral over the parametric domain Ω of the product of a set of n B-spline basis functions $\mathbf{N}$, given by

$$\mathbf{G}_{\mathrm{N,N}} = \left[\int_{\Omega} N_i(x) N_j(x) \mathrm{d}x\right]_{i=1,\dots,n;j=1,\dots,n}. \tag{2.32}$$

In this work, the integration is carried out on an element basis, equivalent to the computation of the mass matrix $\mathbf{M}$ and stiffness matrix $\mathbf{K}$ in Section 2.2.

The resulting Gram matrix is symmetric, block-diagonal and always invertible [29][30][31]. Due to the high continuity of the splines, described in [32], the inverse gramian $\mathbf{G}_{\mathrm{N,N}}^{-1}$ is fully populated. The set of dual basis functions $\boldsymbol{\lambda}$ is then yielded from the linear transformation of the inverse Gram matrix with the associated set of B-spline basis functions, given by

$$\boldsymbol{\lambda}(\xi) = \mathbf{G}_{\mathrm{N,N}}^{-1} \mathbf{N}(\xi). \tag{2.33}$$

Figure 2.2 shows a sample set of inverse gramian dual basis functions $\boldsymbol{\lambda} = \{\lambda_i\}_n$, for $p = 2$ and an open knot vector $\boldsymbol{\Xi} = [0.0, 0.0, 0.0, 0.2, 0.4, 0.6, 0.8, 1.0, 1.0, 1.0]$. The corresponding set of B-splines basis functions $\mathbf{N}$ used for the computation can be seen in Section 2.2 in Figure 2.1.

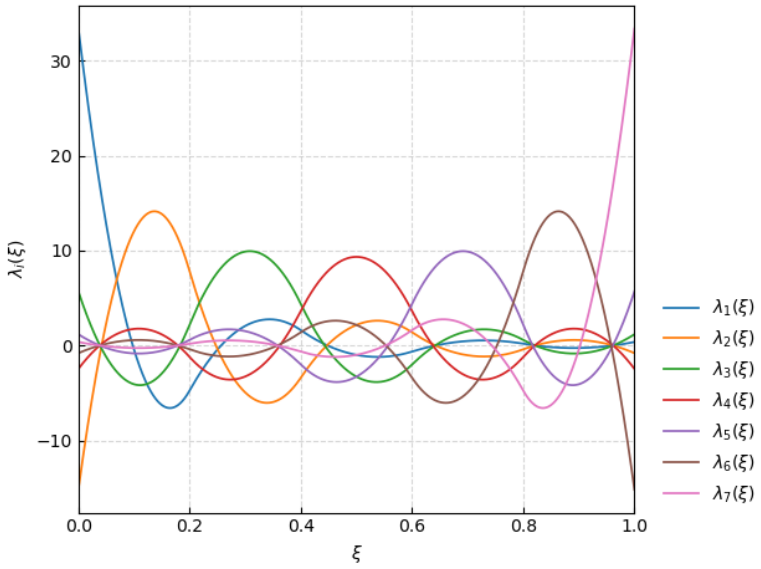

Figure 2.2: Dual basis functions $\boldsymbol{\lambda}$

The support of each resulting dual basis function λ_i is increased to its maximum, i.e., global support [19]. This is caused by the fully populated matrix in Equation (2.33). Moreover, the derived dual basis functions have the optimal degree of reproduction [29] [33].

2.3.2 Approximate dual basis functions

Approximate dual basis functions for B-splines were first introduced by Chui et al. [33] for the context of harmonic analysis. They were also used for the mortar method [19], Held et al. deployed them in [20] for an efficient mass lumping scheme for IGA based on boundary fitted problems and applied for higher-order mass lumping in [17][18].

Approximate dual basis functions are only approximately dual basis functions as implied in their name. Hence, they do not fulfill the property of the dual functional defined in Equation (2.27) completely, only approximately. But more importantly, the required degree of polynomial reproduction $\leq p$ is attained [19]. The approach for the computation of approximate dual basis functions for B-spline basis functions is shown within this section and is derived from [19] [20]. Detailed derivations and mathematical proofs of approximate dual basis functions can be found in [33].

Approximate dual basis functions $\tilde{\boldsymbol{\lambda}}$ with a reproduction degree of $q \leq p$ result from the product of the transformation matrix $\mathbf{S}_q$ and a set of B-spline basis functions $\mathbf{N}$, given by

$$\tilde{\boldsymbol{\lambda}}(\xi) = \mathbf{S}_q(\boldsymbol{\Xi})\mathbf{N}(\xi). \tag{2.34}$$

The banded transformation matrix $\mathbf{S}_q$, with a bandwidth of r, is defined by

$$\boldsymbol{S}_q(\boldsymbol{\Xi}) = \mathbf{U}_{\boldsymbol{\Xi};0} + \sum_{\nu=1}^{q} \left[\left(\prod_{k=1}^{\nu} \mathbf{D}_{\boldsymbol{\Xi};p+k} \right) \mathbf{U}_{\boldsymbol{\Xi};\nu} \left(\prod_{k=1}^{\nu} \mathbf{D}_{\boldsymbol{\Xi};p+k} \right)^T \right]. \tag{2.35}$$

The diagonal matrices $\mathbf{U}_{\boldsymbol{\Xi};\nu}$ have to be computed for $\nu = 0, 1, \ldots, q$

$$\mathbf{U}_{\boldsymbol{\Xi};\nu} = \operatorname{diag}\left[u^{(\nu)}_{\boldsymbol{\Xi};p,1}, \ldots, u^{(\nu)}_{\boldsymbol{\Xi};p,n-\nu} \right]. \tag{2.36}$$

Their entries are all positive and given by

$$u^{(\nu)}_{\boldsymbol{\Xi};p,j} = \frac{p+\nu+1}{\xi_{j+p+\nu+1} - \xi_j} \beta^{(\nu)}_{\boldsymbol{\Xi};p,j}, \tag{2.37}$$

with

$$\beta^{(\nu)}_{\boldsymbol{\Xi};p,j} = \begin{cases} 1 & \nu = 0 \\ \frac{(p+1)!(p-\nu)!}{(p+\nu+1)!(p+\nu)!} F_\nu(\xi_{j+1}, \ldots, \xi_{j+p+\nu}) & 1 \leq \nu \leq q \end{cases}. \tag{2.38}$$

The polynomial function $F_\nu : \mathbb{R}^r \to \mathbb{R}$ is defined as

$$F_\nu(x_1, \ldots, x_r) = \frac{2^{-\nu}}{\nu!} \sum_{\substack{1 \le i_1, \ldots, i_{2\nu} \le r \\ i_1, \ldots, i_{2\nu} \text{ distinct}}} \prod_{j=1}^{\nu} (x_{i_{2j-1}} - x_{i_{2j}})^2. \tag{2.39}$$

Explicit formulas for a more efficient computation of the polynomial F_ν for values of $\nu = 1, \ldots, 5$ [33] are given in the Appendix A.1 and used for the computation within this work. For $r = p+1, \ldots, p+q$ the matrices $\mathbf{D}_{\boldsymbol{\Xi};r}$ are defined by

$$\mathbf{D}_{\boldsymbol{\Xi};r} = \operatorname{diag}[d_{\boldsymbol{\Xi};r,1}, \ldots, d_{\boldsymbol{\Xi};r,n+p+1-r}] \boldsymbol{\Delta}_{n+p+1-r}, \tag{2.40}$$

with the entries of the diagonal matrix as

$$d_{\boldsymbol{\Xi};r,j} = \frac{r}{\xi_{j+r} - \xi_j} \tag{2.41}$$

and a rectangular banded matrix

$$\boldsymbol{\Delta}_s = \begin{bmatrix} 1 & & & \\ -1 & 1 & & \\ & \ddots & \ddots & \\ & & -1 & 1 \\ & & & -1 \end{bmatrix}_{s \times (s-1)}. \tag{2.42}$$

Every matrix $\mathbf{D}_{\boldsymbol{\Xi};r}$ has only two non-zero diagonal entries caused by the multiplication with the rectangular banded matrix in its computation. The bandwidth of the transformation matrix $\mathbf{S}_q$ is therefore given by r and depends only on the reproduction degree q.

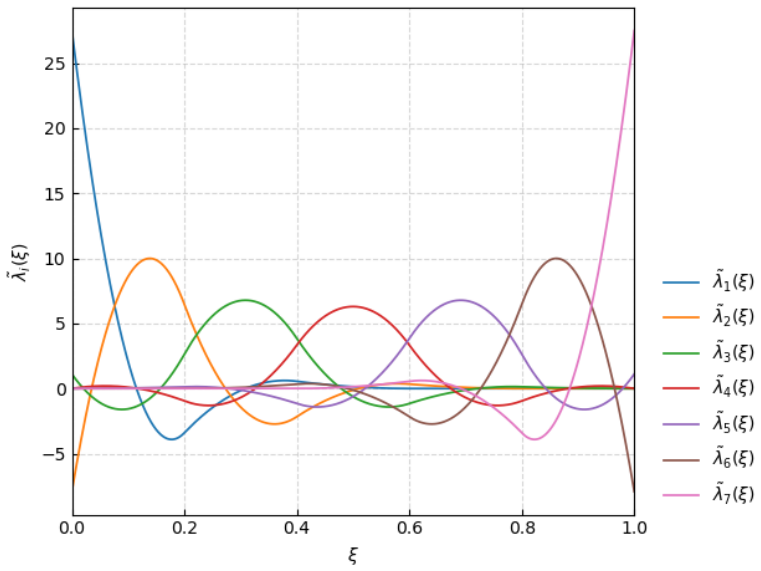

Figure 2.3: Approximate dual basis functions $\tilde{\boldsymbol{\lambda}}$

A sample set of approximate dual basis functions $\tilde{\boldsymbol{\lambda}} = \{\tilde{\lambda}_i\}_n$, with a polynomial degree of $p = 2$, a reproduction degree of $q = 2$ and an open knot vector $\boldsymbol{\Xi} = [0.0, 0.0, 0.0, 0.2, 0.4, 0.6, 0.8, 1.0, 1.0, 1.0]$ is shown in Figure 2.3. Their corresponding set of B-splines basis functions $\mathbf{N}$ can be seen in Section 2.2 in Figure 2.1. It can be observed that the support of each approximate dual basis function $\tilde{\lambda}_i$ is enlarged to $p + 2q + 1$, but remains local [19] [20]. Analogously, each element has $p + 2q + 1$ non-zero approximate dual basis functions. For the maximum degree of reproduction $q = p$, the support is $3p + 1$.

2.4 Finite cell method

The Finite Cell Method (FCM) is a fictitious domain method. The introduction in this section follows [25], [26]. FCM is the other foundational method for the IGA-FCM used in this thesis. The combination of IGA and FCM has already been studied by Rank et al. in the context of linear elasticity [34] and by Bürchner et al. for the wave equation [8].

Accurate generation of a boundary-conforming mesh for complex geometric structures in FEA can be cost intensive or impossible, especially in two- or three-dimensions [25]. FCM simplifies the mesh generation issue by introducing a larger domain in which the physical structure is embedded.

(a) Physical domain **(b)** Meshed embedding domain

Figure 2.4: Two-dimensional FCM example with a Cartesian mesh [25].

An example can be seen in Figure 2.4, in which the physical domain Ω_p is embedded in a lager domain Ω, which is partitioned so that

$$\Omega = \Omega_\mathrm{p} \cup \Omega_\mathrm{f}. \tag{2.43}$$

Ω_f denotes the fictitious domain and a simple Cartesian mesh partitions the domain Ω.

The material of the fictitious domain is scaled down by an indicator function $\alpha(x)$, defined by

$$\alpha(x) = \begin{cases} 1 & x \in \Omega_\mathrm{p} \\ 10^{-\beta} & x \in \Omega_\mathrm{f} \end{cases}. \tag{2.44}$$

To capture the boundary most accurately, it seems plausible to choose $\beta \to \infty$ and therefore $\alpha(x) \to 0$ for $x \in \Omega_\mathrm{f}$. In practice β is set as $\beta \in [3, 10]$ [35] [36], as a too large value may lead to ill conditioning [37]. The density $\rho(x)$ and wave speed $c(x)$ over the whole domain Ω are therefore given by the physical material constants ρ_0 and c_0 as

$$\rho(x) = \alpha(x)\rho_0, \qquad x \in \Omega, \tag{2.45}$$

$$c(x) = c_0, \qquad x \in \Omega. \tag{2.46}$$

The strong form of the elastic wave equation, Equation (2.5), is consequently defined by

$$\alpha(x)\rho_0 \ddot{u}(x,t) + \frac{\partial}{\partial x}\left(\alpha(x)\rho_0 c_0^2 \frac{\partial}{\partial x} u(x,t)\right) = f(x,t), \qquad x \in \Omega, \quad t \in [0, T_\mathrm{max}]. \tag{2.47}$$

When the scaled material properties are substituted into Equations (2.23) to (2.25), the integrals for cut elements, i.e., elements containing the physical and the fictitious domain, are discontinuous, therefore, the integration is split up into two sub-cells. The integration for an arbitrary function $a(x)$, scaled with the indicator function $\alpha(x)$, is given by

$$\int_\Omega \alpha(x) a(x) \mathrm{d}x = \int_{\Omega_p} 1 \cdot a(x) \mathrm{d}x + \int_{\Omega_f} 10^{-\beta} \cdot a(x) \mathrm{d}x. \tag{2.48}$$

Within the work in hand, the boundaries of the one-dimensional domain are known prior, so they are captured precisely. In practice, it can be computationally expensive to obtain an accurate partitioning for two or three-dimensional structures [26]. Hubrich et al. suggested moment fitting and smart octrees [38] to overcome this drawback of FCM.

2.5 Mass lumping

Row-summing is an applied mass lumping method for B-splines, because of their non-negative partition of unity [39]. It can be used for boundary conforming [40] and also to immersed IGA [41][42] to obtain a diagonal mass matrix $\mathbf{M}$.

As the name implies, all entries in one row of the mass matrix $\mathbf{M}$ are summed up. The sum is then written onto the diagonal entry in the corresponding row of the lumped mass matrix $\tilde{\mathbf{M}}$, i.e.,

$$\tilde{M}_{ij} = \begin{cases} \sum_{j=1}^{n} M_{ij} & \text{if} \quad i = j \\ 0 & \text{otherwise} \end{cases} . \tag{2.49}$$

Row-summing can be applied to all rows of the mass matrix, fully lumped, or just to specific rows, partially lumped. In partially lumped mass matrices, rows that are not lumped are identical to the ones in the initial mass matrices.

For this work, it is important to denote that the mass matrices are partially lumped for the IGA-FCM approach with approximate dual basis functions as test functions. Row-summing is applied only to those rows of the mass matrix $\mathbf{M}$, where the corresponding test functions have no support in the cut elements. Row-summing of the rows associated with the cut elements can lead to negative entries on the diagonal and cause numerical instability. This was observed in [25] for the Spectral Cell Method (SCM). The detailed introduction of the immersed problem studied in this thesis is given in Chapter 3.

Chapter 3

Numerical Investigations

3.1 Problem statement

In this thesis, a one-dimensional immersed problem is assumed and discretized by the Isogeometric Finite Cell Analysis (IGA-FCM). The spatial domain $\Omega = [x_{\min}, x_{\min}]$ is symmetrical about the origin, $x = 0$, and has its limits at $x_{\min} = -2.0$ and $x_{\max} = 2.0$. An elastic bar, with a length of $l = 3.268$, is placed in the domain Ω with its middle in the origin. So the ends of the bar lie at $x_{\mathrm{l}} = -1.634$ and $x_{\mathrm{r}} = 1.634$. The domain Ω is divided into the fictitious domain Ω_{f} and the physical domain Ω_{p}, this can be seen in Figure 3.1 and is defined by

$$\Omega_{\mathrm{f}} = [-2, -1.634) \cup (1.634, 2.0], \tag{3.1}$$

$$\Omega_{\mathrm{p}} = [-1.634, 1.634]. \tag{3.2}$$

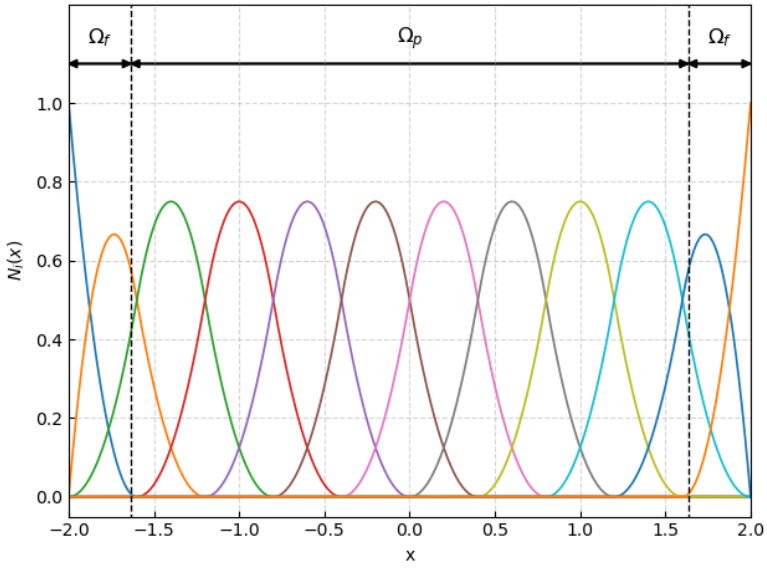

Figure 3.1: Partition of the spatial domain Ω

The material of the bar is assumed to be isotropic and homogeneous. Thus, the wave speed and density are constants $c_0 = 1$ and $\rho_0 = 1$. For the indicator function $\alpha(x)$, the factor β is set to $\beta = 10$. Therefore the wave speed is $c_0 = 1$ for whole domain Ω and the scaled density is

$$\alpha(x)\rho_0 = \begin{cases} 1 & x \in \Omega_{\mathrm{p}} \\ 1 \cdot 10^{-10} & x \in \Omega_{\mathrm{f}} \end{cases}. \tag{3.3}$$

The numerical investigations are focused on the accuracy of the discretization for this immersed problem by the IGA-FCM for approaches with different sets of basis functions used to approximate the test function. Dual and approximate dual basis functions $\boldsymbol{\lambda}$ are deployed in the test function for the Petrov-Galerkin method and are benchmarked against the Bubnov-Galerkin method, where B-spline basis functions $\mathbf{N}$ are used. For the Petrov-Galerkin method, the approximation for the test function $\tilde{v}(x)$ defined in Equation (2.13), is given by

$$v(x) \approx \tilde{v}(x) = \sum_{i=1}^{n} \lambda_i(x)\hat{v}_i \tag{3.4}$$

and the approximation of the wave field $\tilde{u}(x,t)$, see Equation (2.12), remains unchanged. This definition change must be considered for all Equations (2.14) to (2.25) for the Petrov-Galerkin method. The basis functions used for the approximation of the wave field are referred to as ansatz functions, and the basis functions applied for the approximation of the test function directly as test functions. The notation for all combinations of basis functions, with and without mass lumping, can be found in Table 3.1.

Table 3.1: Investigated approaches: combinations of ansatz functions, test functions and mass lumping

Notation	Ansatz Functions		Test Functions		Mass Lumping
c-IGA-FCM	B-splines	$\mathbf{N}$	B-splines	$\mathbf{N}$	None
l-IGA-FCM	B-splines	$\mathbf{N}$	B-splines	$\mathbf{N}$	Full
c-IGA-FCM-D	B-splines	$\mathbf{N}$	Dual	$\boldsymbol{\lambda}$	None
c-IGA-FCM-AD	B-splines	$\mathbf{N}$	Approximate Dual	$\tilde{\boldsymbol{\lambda}}$	None
l-IGA-FCM-AD	B-splines	$\mathbf{N}$	Approximate Dual	$\tilde{\boldsymbol{\lambda}}$	Partial

Row-summing is this work's mass lumping scheme of choice and was introduced in Chapter 2. For the notations in Table 3.1, the c is short for consistent and the l for lumped. They refer to the mass matrix $\mathbf{M}$. Mass lumping is applied only to the B-spline and approximate dual approach. For l-IGA-FCM, all rows of the mass matrix are row-summed, i.e., the fully lumped. For the mass matrix of l-IGA-FCM-AD, row summing is just applied to those rows where the corresponding test functions have no support in the cut elements, i.e., partially lumped.

Furthermore, it has to be denoted that the polynomial degree of reproduction q for the approximate dual test functions is always at its maximum, i.e., $q = p$, where p denotes the polynomial degree of the B-spline ansatz functions.

Every integration in this chapter is carried out with the GL integration scheme on an element basis, and each element has $n_{\text{int}} = p + 1$ integration points. For cut elements according to their fill ratio, the integration points are split up for the two sub-elements.

3.2 Asymptotic accuracy

A convergence study is performed in this section to quantify the asymptotic accuracy for all IGA-FCM approaches introduced in Section 3.1. Two errors are computed for linear up to quadratic C^{p-1} B-splines and their test functions for a varied element size h. The error measures in this section are derived from [43].

The first error is the relative difference between a set discrete eigenfrequency ω_i^h and its reference solution ω_i. The second error is the difference of the corresponding discrete eigenvector $\hat{u}_i^h$ relative to its reference solution $\hat{u}_i$. The reference solutions are computed analytically and are defined by

$$\omega_i = \frac{i\pi}{L - 2\zeta}, \tag{3.5}$$

$$\hat{u}_i(x) = \sqrt{\frac{2}{L - 2\zeta}}\cos(\omega_i x). \tag{3.6}$$

Hereby, L denotes the length of the spatial domain Ω and ζ the length of the fictitious domain Ω_f on each side of the bar. For the introduced numerical problem, they are set to

$$L = |x_\mathrm{min}| + x_\mathrm{max} = 4, \tag{3.7}$$

$$\zeta = |x_\mathrm{min}| - |x_\mathrm{l}| = x_\mathrm{max} - x_\mathrm{r} = 2 - 1.634 = 0.366. \tag{3.8}$$

To obtain any discrete eigenfrequency and corresponding eigenvector, the generalized eigenvalue problem [39] has to be solved first and is given by

$$(\mathbf{K} - \lambda_i^h \mathbf{M})\hat{\mathbf{u}}_i = 0. \tag{3.9}$$

The matrices $\mathbf{M}$ and $\mathbf{K}$ are derived from the space-discrete form of the elastic wave equation, see Equation (2.16) and λ_i^h denotes the i'th discrete eigenvalue. The i'th eigenfrequency ω_i^h and eigenvector $\hat{u}_i^h$ are then given by

$$\omega_i^h = \sqrt{\lambda_i^h}, \tag{3.10}$$

$$\hat{u}_i^h(x) = \mathbf{N}(x)\hat{\mathbf{u}}_i. \tag{3.11}$$

The error for the eigenfrequency e_{ω_i} and for the corresponding eigengenvector $e_{\hat{u}_i}$, using the L_2-norm, are given by

$$e_{\omega_i} = \left|\frac{\omega_i^h - \omega_i}{\omega_i}\right|, \tag{3.12}$$

$$e_{\hat{u}_i} = \min_{s\in\{-1,+1\}} \sqrt{\frac{\int_{x_l}^{x_r}(\hat{u}_i^h(x,t) - s\hat{u}_i(x,t))^2 \mathrm{d}x}{\int_{x_l}^{x_r}(\hat{u}_i(x,t))^2 \mathrm{d}x}}. \tag{3.13}$$

The quadrature points used for the L_2-norm are identical to the points of the GL integration of the weak form in Equation (2.14). Furthermore the discrete eigenvector is normalized $||\hat{u}_i^h|| = ||\hat{u}_i|| = 1$, so the error is relative. The value of s ensures that the right sign is always used for the computation of the reference eigenvector.

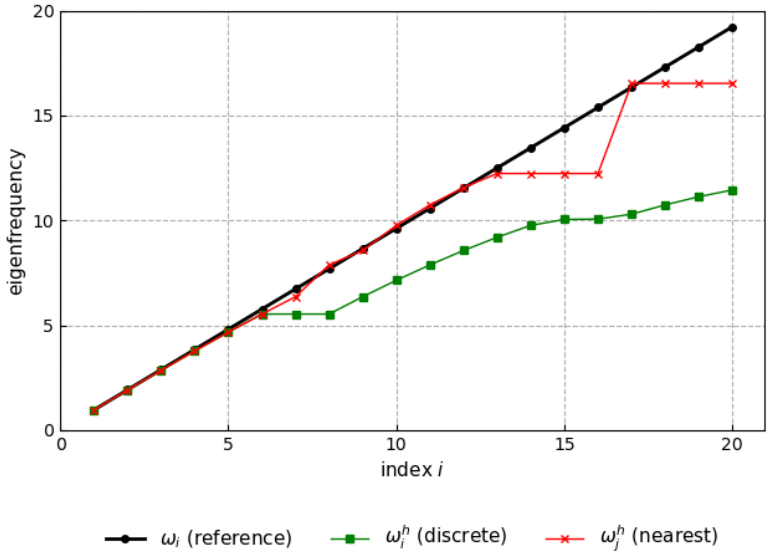

Figure 3.2: Exact and discrete eigenfrequency spectrum of the first 20 modes for I-IGA-FCM with $p = 2$ and $h = \frac{4}{40}$.

For immersed boundary problems with lumped mass matrices, non-physical spurious modes can enter the discrete spectrum [43]. Due to this, the relative errors defined in Equations (3.12) and (3.13) are not directly used. To overcome this issue, the nearest discrete solution ω_j^h to the reference solution ω_i is searched first in the whole discrete spectrum, exemplary visualized in Figure 3.2, and then used for the computation. Therefore, the errors are defined by

$$e_{\omega_i} = \min_j \left| \frac{\omega_j^h - \omega_i}{\omega_i} \right|, \tag{3.14}$$

$$e_{\hat{u}_i} = \min_j \min_{s\in\{-1,+1\}} \sqrt{\frac{\int_{x_l}^{x_r} (\hat{u}_j^h(x,t) - s\hat{u}_i(x,t))^2 \mathrm{d}x}{\int_{x_l}^{x_r} (\hat{u}_i(x,t))^2 \mathrm{d}x}} \tag{3.15}$$

and will always yield a minimum for the set i'th mode. It has to be denoted that the index j is always identical for the discrete eigenfrequency and eigenvector. For eigenfrequencies on the far left of the spectrum, $j = i$ holds true. This can be observed in Figure 3.2. On the downside, the minor modes converge faster against the machine precision [43]. Considering this, the mode for the convergence study for the asymptotic accuracy in this thesis is set to $i = 4$.

The errors e_{ω_4} and $e_{\hat{u}_i}$ are computed for all IGA-FCM approaches, for polynomial degrees of $p = 1, 2, 3, 4$ and a varied element size $h = \frac{4}{10}, \frac{4}{20}, \frac{4}{40}, \frac{4}{80}, \frac{4}{160}, \frac{4}{320}$. The convergence of those errors can be seen in Figures 3.3 to 3.7.

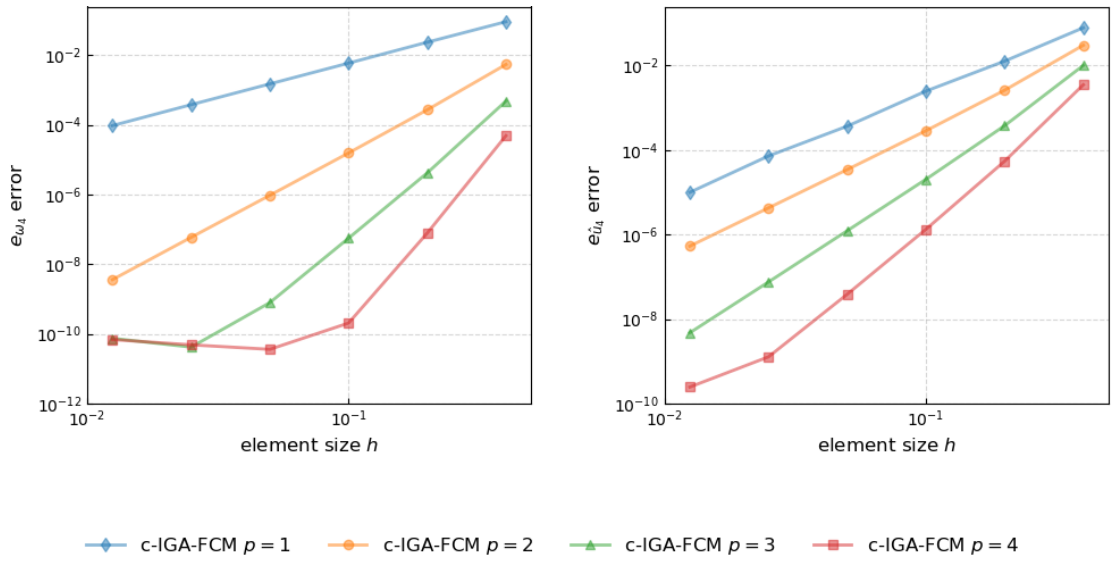

Figure 3.3: Asymptotic accuracy of c-IGA-FCM: On the left convergence of the fourth eigenfrequency and on right convergence of the fourth eigenvector.

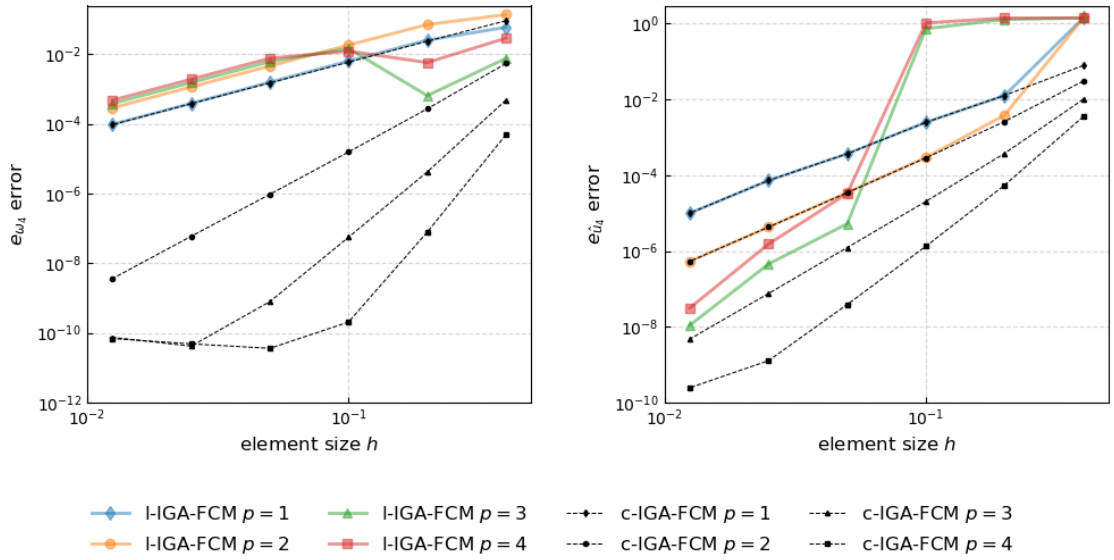

Figure 3.4: Asymptotic accuracy of l-IGA-FCM: On the left convergence of the fourth eigenfrequency and on right convergence of the fourth eigenvector.

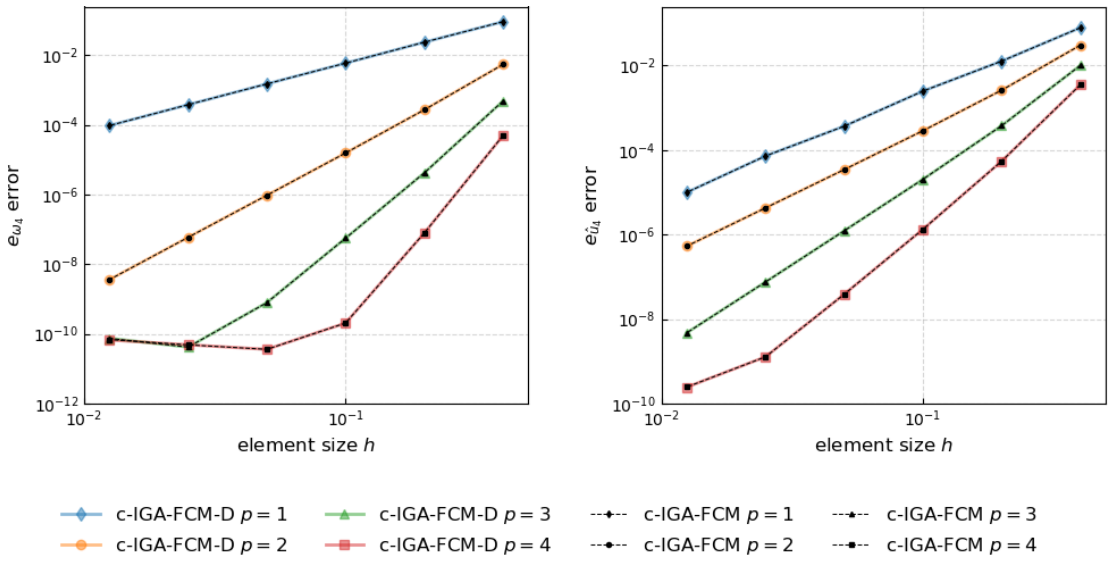

Figure 3.5: Asymptotic accuracy of c-IGA-FCM-D: On the left convergence of the fourth eigenfrequency and on right convergence of the fourth eigenvector.

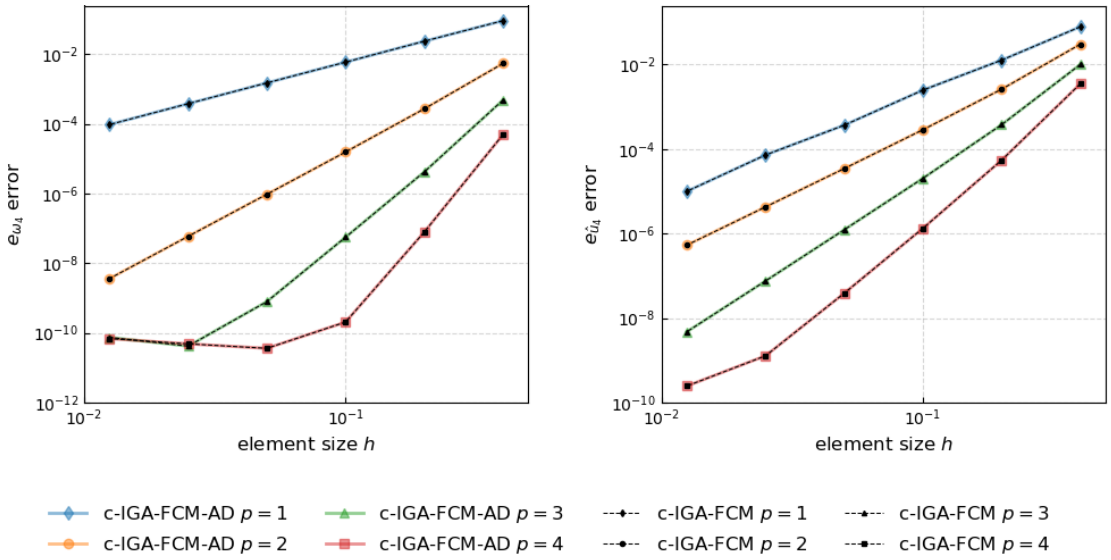

Figure 3.6: Asymptotic accuracy of c-IGA-FCM-AD: On the left convergence of the fourth eigenfrequency and on right convergence of the fourth eigenvector.

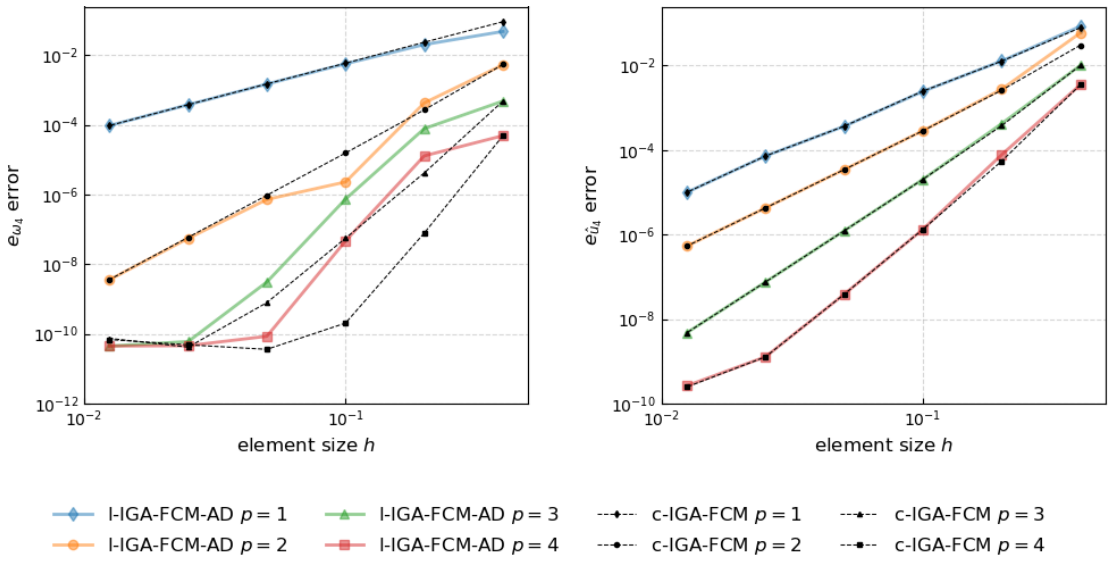

Figure 3.7: Asymptotic accuracy of l-IGA-FCM-AD: On the left convergence of the fourth eigenfrequency and on right convergence of the fourth eigenvector.

3.3 Wave propagation

This section introduces the transient problem for the system of Section 3.1. All parameters defined in Section 3.1 remain unchanged. The propagation of an elastic wave in the bar is assumed. Analogously to the master thesis of Fassbender [26], the reference displacement of the elastic wave $u(x,t)$ is modeled by two Gaussian waves. They are defined by

$$u(x,t)_{\text{ref}} = u_l(x,t) + u_r(x,t), \tag{3.16}$$

$$u_l(x,t) = e^{-\frac{(x+ct)^2}{2\sigma^2}}, \tag{3.17}$$

$$u_r(x,t) = e^{-\frac{(x-ct)^2}{2\sigma^2}}. \tag{3.18}$$

Each Gauss wave is defined individually in Equation (3.17) and (3.18) because their direction of propagation is different. The indices describe the initial direction as left and right of the origin $x = 0$. The wave speed is denoted by c and is set to $c = 1$ for the purpose of this work. The standard derivation σ of the Gaussian wave is given by

$$\sigma = \frac{\lambda_{\text{dom}}}{2\pi} \qquad \text{with} \qquad \lambda_{\text{dom}} = \frac{c}{f}. \tag{3.19}$$

The frequency f is set to $f = 1$, ergo the dominant wavelength is $\lambda_{\text{dom}} = 1$ and the standard derivation $\sigma = \frac{1}{2\pi}$.

For the time integration of the space-discrete form of the elastic wave equation, see Equation (2.16), the second-order Central Difference Method (CDM) is applied. CDM is an explicit and conditionally stable time integration scheme [8]. The next time step

$t_{i+1} = t_i + \Delta t$ is computed from the previous two time steps, t_i and $t_{i-1} = t_i - \Delta t$. The time discretization is given by

$$\hat{\mathbf{u}}(t_{i+1}) = 2\hat{\mathbf{u}}(t_i) - \hat{\mathbf{u}}(t_{i-1}) + \Delta t^2 \mathbf{M}^{-1} \left[\hat{\mathbf{f}}(t_i) - \mathbf{K}\hat{\mathbf{u}}(t_i) \right]. \tag{3.20}$$

To yield the critical time step Δt_{crit} of the CDM discretization, first the generalized eigenvalue problem, see Equation (3.9), is solved to receive the largest eigenvalue $\lambda_{\max}$ and is then given as

$$\Delta t_{\text{crit}} = \frac{2}{\sqrt{\lambda_{\max}}}. \tag{3.21}$$

The one-dimensional Neumann boundary conditions for the elastic wave and the initial conditions for the time integration by the reference solution for $t = 0$ and $t = -\Delta t$ are defined by

$$u_{\text{ref}}(x, 0) = 2e^{-\frac{(x)^2}{2\sigma^2}}, \qquad x \in \Omega, \tag{3.22}$$

$$u_{\text{ref}}(x, -\Delta t) = e^{-\frac{(x-c\Delta t)^2}{2\sigma^2}} + e^{-\frac{(x+c\Delta t)^2}{2\sigma^2}}, \qquad x \in \Omega, \tag{3.23}$$

$$\frac{\partial}{\partial x} u(x, t) = 0, \qquad x \in \partial\Omega, \quad t \in [0, T_{\max}]. \tag{3.24}$$

Both ends of the bar are free, i.e., not supported, so no Dirichlet boundary conditions are applied.

3.4 Transient accuracy

To determine the accuracy of all IGA-FCM approaches discretising the transient problem, defined in section 3.3, an adequate error measurement must be found.

The initial condition for the displacement of the elastic wave is given in Equation 3.22, as the superposition of the two Gaussian waves with the amplitude peak at $x = 0$. Then, each Gaussian wave propagates outwards to one interface of the bar, where they get reflected backwards due to the Neumann boundary conditions defined in Equation (3.24). After each Gaussian wave travelled a distance of $2 \cdot \frac{l}{2}$ they form a superposition with the peak of the amplitude again at the same position as for the initial condition $u_{\text{ref}}(x, 0)$. This can be observed in Figure 3.8. The time required is defined by the travelled distance $l = 3.268$ and wave speed $c = 1$ as

$$T_{\max} = \frac{l}{c} = 3.268. \tag{3.25}$$

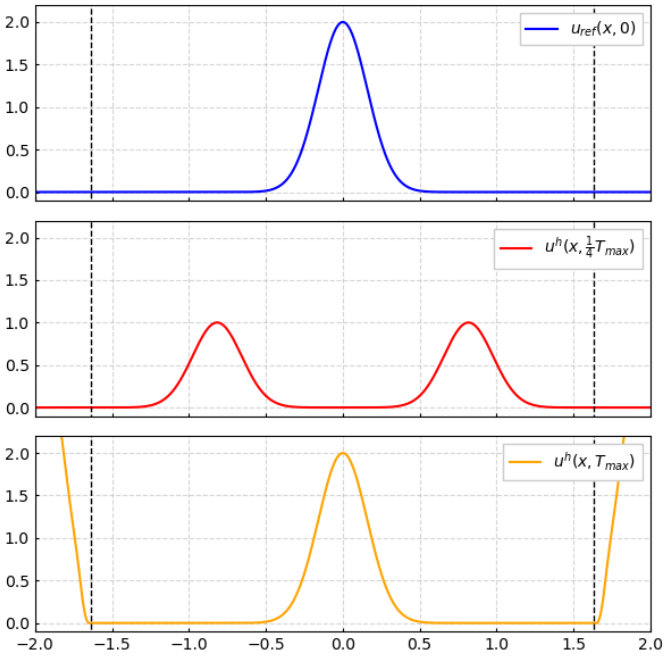

Figure 3.8: Propagation of the elastic wave.

Therefore, the error of the discretization of the transient problem for all IGA-FCM approaches is computed as the relative difference of the initial displacement $u_{\text{ref}}(x, 0)$ at the time $t = 0$ to the discrete displacement $u^h(x, t)$ at the time $t = T_{\text{max}}$. For this error, the relative L_2-norm is deploy and is defined by

$$L_2 = \sqrt{\frac{\int_{x_l}^{x_r} (u^h(x, T_{\text{max}}) - u_{\text{ref}}(x, 0))^2 \mathrm{d}x}{\int_{x_l}^{x_r} (u_{\text{ref}}(x, 0))^2 \mathrm{d}x}}. \tag{3.26}$$

The quadrature points used for the L_2-norm are identical to the ones of the GL integration of the weak form in Equation (2.14). For the computation of discrete solution $u^h(x, t)$ at the time $t = T_{\text{max}}$, the CDM is carried out with $n^t = 10\,000$ time steps for all polynomial degrees p and element sizes h. Because the indicator function is $\alpha(x) \neq 0$, there is a solution outside of the physical domain at the time T_{max}, which can be seen in Figure 3.8. This solution is neglected in the error since it has no physical interpretation.

The L_2 error is computed for all versions of IGA-FCM, for the discretization of the transient problem, for polynomial degrees of $p = 1, 2, 3, 4$ and a varied element size $h = \frac{4}{10}, \frac{4}{20}, \frac{4}{40}, \frac{4}{80}, \frac{4}{160}, \frac{4}{320}$. The convergence of the error for all approaches can be seen in Figures 3.9 to 3.13.

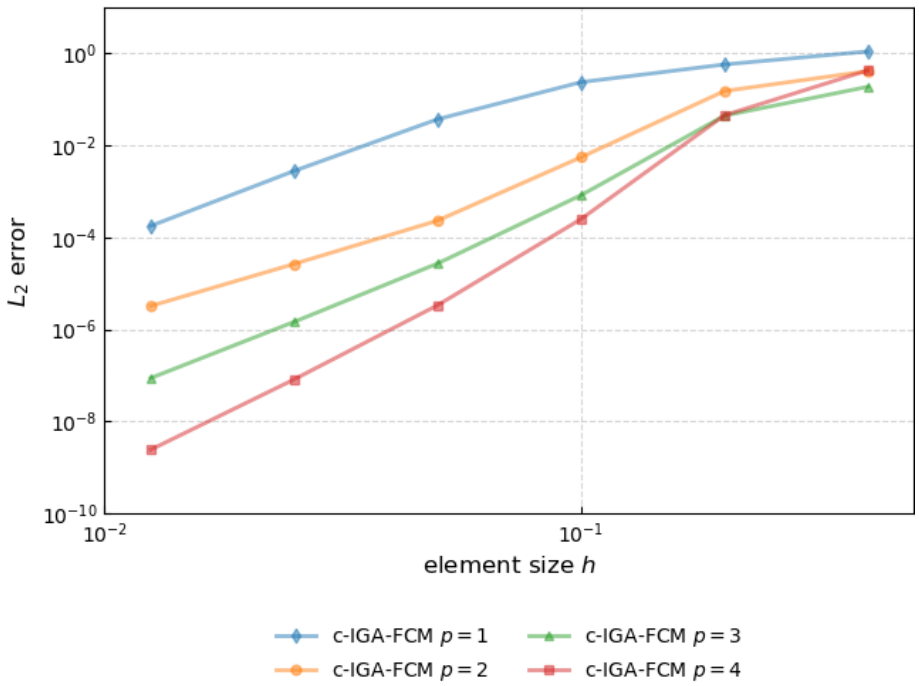

Figure 3.9: Transient accuracy of c-IGA-FCM: Convergence of the L_2 error.

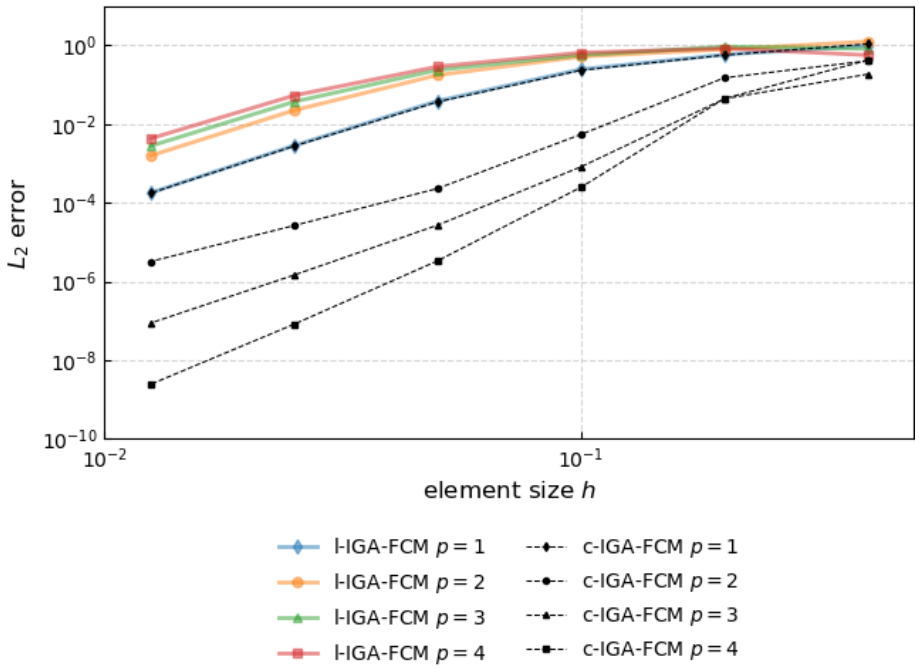

Figure 3.10: Transient accuracy of l-IGA-FCM: Convergence of the L_2 error.

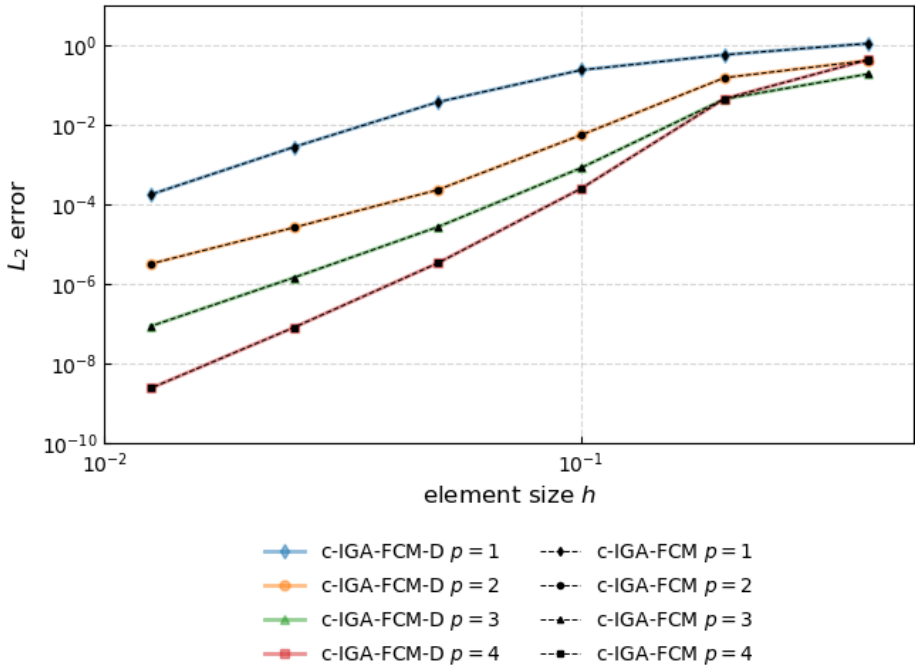

Figure 3.11: Transient accuracy of c-IGA-FCM-D: Convergence of the L_2 error.

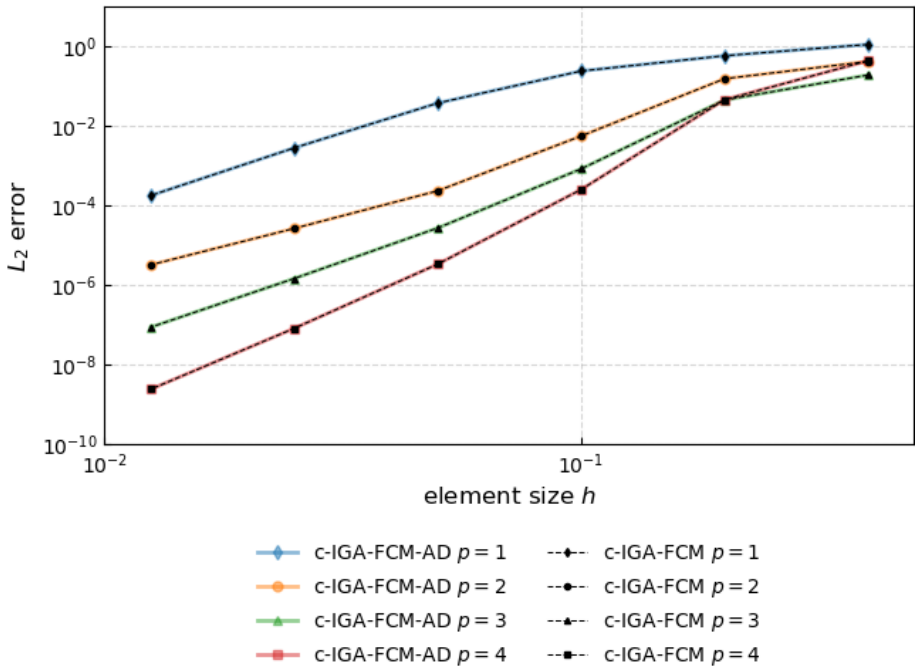

Figure 3.12: Transient accuracy of c-IGA-FCM-AD: Convergence of the L_2 error.

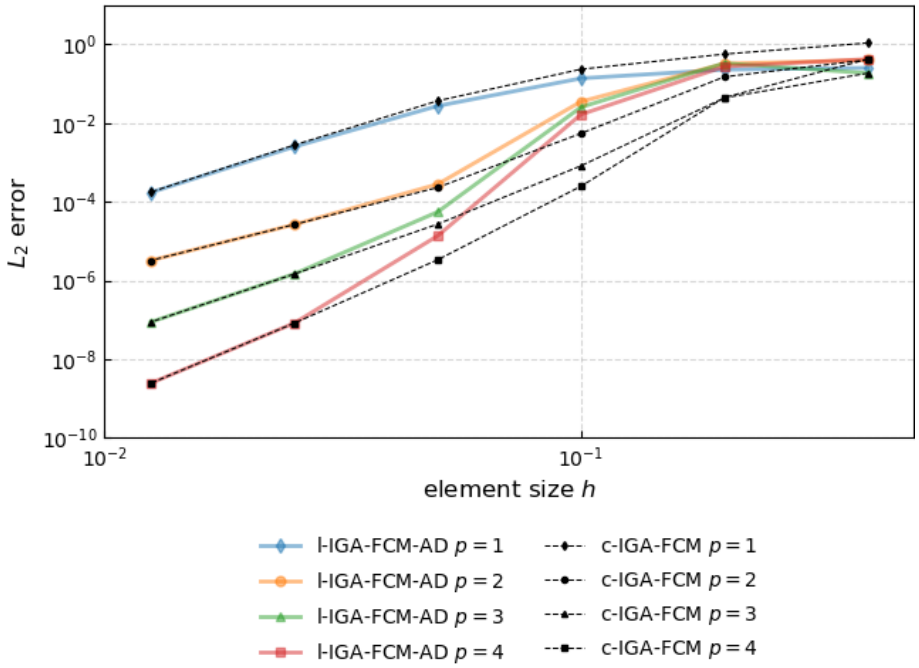

Figure 3.13: Transient accuracy of l-IGA-FCM-AD: Convergence of the L_2 error.

3.5 Discussion

The following analyses and discusses the asymptotic and transient accuracy results of the investigated IGA-FCM approaches. All plots for the relative errors e_{ω_4}, of the fourth eigenfrequency, and $e_{\hat{u}_i}$, of the corresponding fourth eigenvector, of the asymptotic accuracy can be found in Section 3.2. The plots of the L_2 error norm for the transient accuracy are included in Section 3.4.

3.5.1 c-IGA-FCM

For the c-IGA-FCM approach, the Bubnov-Galerkin scheme is used, i.e., the ansatz and test functions are both B-spline basis functions. No mass lumping is deployed to the discrete mass matrix. The asymptotic and transient properties of the c-IGA-FCM will be used as a benchmark relative to all other IGA-FCM approaches.

The error measures for the asymptotic accuracy of c-IGA-FCM can be found in Figure 3.3. For the eigenfrequency on the left and the eigenvector on the right, the convergence rate increases for a higher polynomial degree p. The flattening of the convergence curves for $p = 3, 4$ of the eigenfrequency error at approximately 10^{-10} is most likely associated with a consistency error of the immersed problem. This could be caused by $\beta = -10$, as the factor set for the indicator function $\alpha(x)$. It is assumed that the same applies to the result of the $e_{\hat{u}_4}$ error for $p = 4$ and $h = \frac{4}{320}$. For the transient accuracy in Figure 3.9, a similar behaviour is observed for an increase in the polynomial degree, but no consistency error is obtained. Overall, it can be stated that an increase in the polynomial degree outperformed

the mesh refinement and yielded a more accurate asymptotic and transient accuracy. Comparable results were already found in convergence studies for boundary conforming problems for IGA in [40] [7].

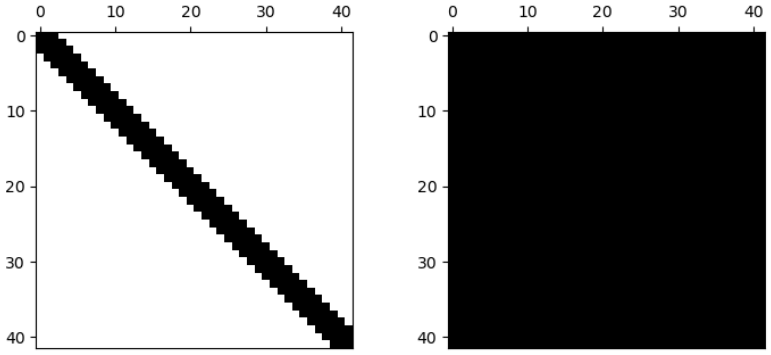

Figure 3.14: Structure of the mass matrix $\mathbf{M}$ (left) and inverse mass matrix $\mathbf{M}^{-1}$ (right) of c-IGA-FCM with $p = 2$ and $h = \frac{4}{40}$.

The resulting mass matrices have a diagonal banded structure, with a bandwidth of $1 + 2p$, shown in Figure 3.14. Due to this, the inverse mass matrices are fully populated, which requires a maximum memory capacity.

3.5.2 l-IGA-FCM

The Bubnov-Galerkin scheme is also applied for the l-IGA-FCM approach, but additionally, row-summing is deployed to all rows of the discrete mass matrix.

Figures 3.4 and 3.9 show that the p-convergence of the eigenfrequency error and the transient error is lost. Moreover, the magnitude of the relative error increases with each increase in the polynomial degree. Similar results for the transient accuracy were also obtained in [8], where IGA-FCM was studied for the FWI. For the eigenvector error, the convergence rate for $p = 1, 2$ is identical to c-IGA-FCM. For higher polynomial degrees, the accuracy relative to c-IGA-FCM is lost.

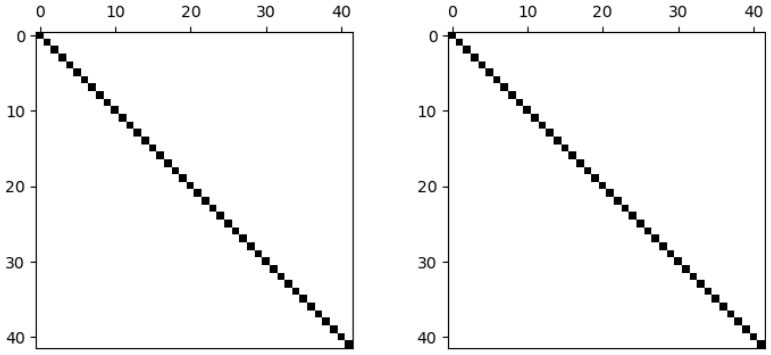

Figure 3.15: Structure of the mass matrix $\mathbf{M}$ (left) and inverse mass matrix $\mathbf{M}^{-1}$ (right) of l-IGA-FCM with $p = 2$ and $h = \frac{4}{40}$.

The resulting mass matrices and inverse mass matrices are diagonal due to the mass lumping and are shown in Figure 3.15. Because mass matrices of such a structure yield smaller largest eigenvalues $\lambda_{\max}$ [18], the critical time step Δt_{crit} for the CDM is greater.

Overall, the accuracy of the l-IGA-FCM is poor, and the advantages for a more efficient computation due to the matrix structure do not outweigh this. So, this approach is not suitable for a wave simulation.

3.5.3 c-IGA-FCM-D

For the c-IGA-FCM-D approach, the ansatz functions are B-spline basis functions and the test functions are dual basis functions. Therefore, the Petrov-Galerkin method is applied. Mass lumping is not deployed to the discrete mass matrix.

The errors obtained for this approach's asymptotic and transient accuracy can be perceived in Figures 3.5 and 3.11. All results attained for c-IGA-FCM-D are identical to the corresponding ones of c-IGA-FCM. So, the increase of the polynomial degree p outperforms the mesh refinement and therefore, this approach is suitable for an accurate wave simulation.

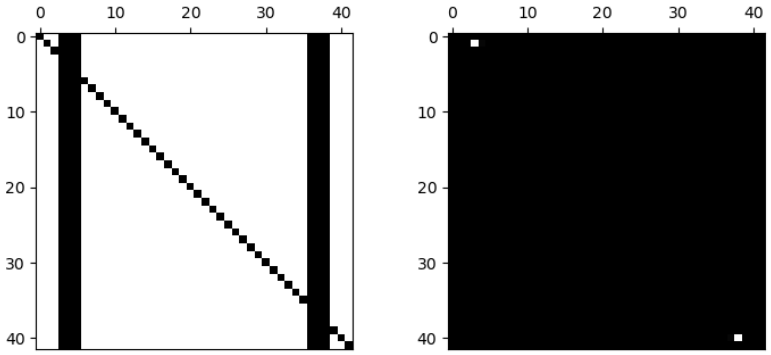

Figure 3.16: Structure of the mass matrix $\mathbf{M}$ (left) and inverse mass matrix $\mathbf{M}^{-1}$ (right) of c-IGA-FCM-D with $p = 2$ and $h = \frac{4}{40}$.

The resulting mass matrices should be diagonal due to the duality relation defined in Equation (2.30). However, it is observed in Figure 3.16 that this does not hold true for the non-boundary conforming problem. The columns corresponding to the ansatz functions defined in the cut elements are fully populated. Hence, the inverse mass matrices show no significant reduction in the population. Besides this are the stiffness matrices $\mathbf{K}$ fully populated due to the global support of the dual test functions [21].

c-IGA-FCM-D can be applied to accurately discretize non-boundary conforming elastic problems but is computationally expensive and requires large memory capacities for the two discrete matrices $\mathbf{M}^{-1}$ and $\mathbf{K}$.

3.5.4 c-IGA-FCM-AD

The Petrov-Galerkin method is also used for the c-IGA-FCM-AD approach. However, approximate dual basis functions are now deployed as test functions. These test functions preserve the properties of the B-spline ansatz functions, such as the local support, smoothness and degree of polynomial reproduction [18][19]. No mass lumping is deployed to the discrete mass matrix.

The relative errors and their convergence rates are shown in Figure 3.6 for the asymptotic and Figure 3.12 for transient accuracy. Analogously to c-IGA-FCM-D, the results of c-IGA-FCM-AD are identical to the c-IGA-FCM approach. The same behavior for the p-refinement out performing the h-refinement applies and qualifies this approach for an accurate wave simulation.

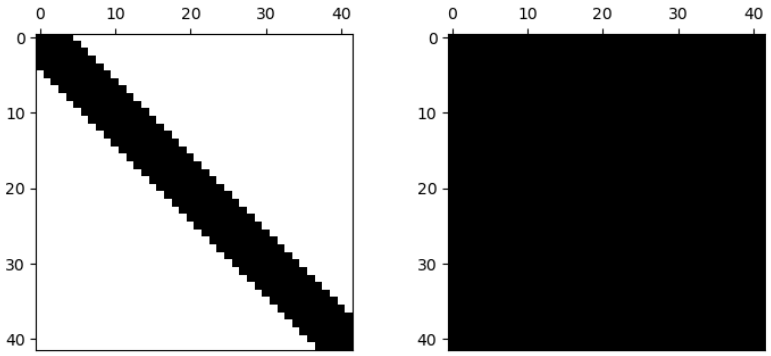

Figure 3.17: Structure of the mass matrix $\mathbf{M}$ (left) and inverse mass matrix $\mathbf{M}^{-1}$ (right) of c-IGA-FCM-AD with $p = 2$ and $h = \frac{4}{40}$.

The diagonal banded structure of the discrete mass matrix can be seen in Figure 3.17. The bandwidth of the matrix is equal to $4p + 1$ for the maximum degree of polynomial reproduction $q = p$. A bandwidth of ≥ 2 does lead to a fully populated inverse mass matrix and can be noticed in Figure 3.17.

Besides their good accuracy, has the c-IGA-FCM-AD approach no further advantages. The computation with fully populated inverse mass matrices requires higher memory capacities and is cost intensive, analogously to c-IGA-FCM-D.

3.5.5 l-IGA-FCM-AD

For l-IGA-FCM-AD, the Petrov-Galerkin method is also applied, with B-spline ansatz functions and approximate dual test functions. Furthermore, partial mass lumping is deployed for the discrete mass matrix. The rows of the mass matrices are only row-summed when the corresponding approximate dual test functions are not supported in the cut elements. This approach is the most promising for the context of this thesis.

The asymptotic accuracy of the fourth eigenfrequency and eigenvector can be seen in Figure 3.7. For the e_{ω_4} error, the convergence curves of $p = 1, 2$ are similar to the corresponding ones of c-IGA-FCM. On the other hand, the results of $p = 3, 4$ show a more significant divergence, especially in the error magnitude. But it is important to denote that overall, the p-convergence is not lost, i.e., a higher polynomial degree yields a higher convergence. The magnitudes for the $e_{\hat{u}_4}$ error are, besides some small divergences on the right, nearly identical to the ones of c-IGA-FCM. But more importantly, they have the same convergence rates. A pre-asymptotic behaviour can be perceived for the global accuracy of l-IGA-FCM-AD in Figure 3.13. For larger element sizes on the right, the relative error is high regardless of polynomial degree. With the increase of the mesh refinement, the convergence of each polynomial degree increases till they reach the same rate and also the same magnitude as their equivalent one of the c-IGA-FCM approach. This demonstrates that l-IGA-FCM-AD is a suitable approach for an accurate wave simulation when the element sizes are under a certain threshold, i.e., outside of the pre-asymptotic area.

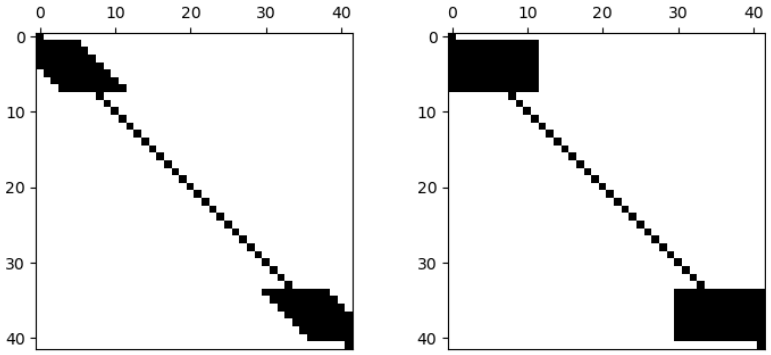

Figure 3.18: Structure of the mass matrix $\mathbf{M}$ (left) and inverse mass matrix $\mathbf{M}^{-1}$ (right) of l-IGA-FCM-AD with $p = 2$ and $h = \frac{4}{40}$.

Due to the partial mass lumping, the structure of the resulting mass matrices is partially diagonal, with two populated blocks corresponding to the cut elements. This can be seen in Figure 3.18. Such a mass matrix structure would allow the utilization of an IMEX time integration approach. Therefore, only the populated blocks must be inverted to obtain the inverse mass matrix. However, for the frame of this thesis, only an explicit time integration scheme is used.

The l-IGA-FCM-AD approach yields a good accuracy of the wave simulation for small element sizes and the properties of the c-IGA-FCM approach, such as the p-convergence, are attained. More soever, the inverse mass matrices $\mathbf{M}^{-1}$ are significantly less populated and therefore require less memory capacity for the computation.

Chapter 4

Conclusion

4.1 Summary

In this thesis, different IGA-FCM approaches were presented to discretize the one-dimensional wave equation in an immersed problem setting. Therefore, the Bubnov-Galerkin method, with B-spline test functions, and the Petrov-Galerkin method, with dual and approximate dual test functions, were used with and without mass lumping. IGA is a higher-order FEM that is well known for its high convergence rates and precision with a low number of dof [1][7] and in this work B-spline basis functions were utilized as ansatz functions. The combination with the FCM allowed the generation of a simple mesh for the non-boundary conforming problem.

It was observed in Chapter 3 that all discretization approaches without mass lumping, i.e., consistent mass matrices, of the IGA-FCM yielded the same error magnitude and convergence rates for the asymptotic and transient accuracy. Due to the discontinuous material domain of the immersed problem, the bi-orthogonality of the dual test functions was lost in the cut elements and the inverse mass matrix was fully populated. The approximate dual test functions have local support [33], analogously to the B-spline test functions, yielding fully populated inverse mass matrices. Both approaches with the Petrov-Galerkin method do not increase the efficiency of the computation.

For IGA-FCM with B-spline test functions and approximate dual test functions, row-summing was applied. The results of the Bubnov-Galerkin method with full row-summing showed the same poor behaviour as in [8]. The p-convergence is lost and the relative magnitude increases for an increase of polynomial degree for the error of the eigenfrequency and the transient accuracy. On the other hand, the approximate dual test functions, with partial row-summing, showed more promising results. They attained the same accuracy for small element sizes, so a higher number of dof, as the discretization with B-spline test functions without mass lumping. The structure of the resulting partially lumped mass matrices can be seen in Figure 3.18 and is such that it would allow an IMEX time integration approach to discretize the transient problem in the time. However, in this thesis, only an explicit time integration scheme was used.

4.2 Outlook

Based on the results of this thesis, potential additions and future investigations for IGA-FCM are outlined in this section.

4.2.1 Implicit-Explicit time integration scheme

As already mentioned in this work, the structure of the mass matrix and its inverse for lumped IGA-FCM with approximate dual basis functions would allow the utilization of an Implicit-Explicit (IMEX) time integration scheme. IMEX methods were studied by Fassbender in his master thesis in [26] and in [16], for a wave propagation problem with the Spectral Cell Method (SCM). The properties of an IMEX integration scheme in this section are derived from [26][16].

For an IMEX time integration method, the partially lumped mass matrix is partitioned into the diagonal part, where all elements lie within the physical domain and the part for the cut elements. The diagonal part is then integrated by an explicit conditionally stable time integration method, such as the Central Difference Method (CDM), and the other part is integrated by an implicit unconditionally stable time integration method, e.g., trapezoidal. Different implicit time integration methods can be found in [26].

The advantage of this method is that an implicit time integration method is unconditionally stable, i.e., it does not depend on a critical time step. It, therefore, yields accurate results for all time step sizes. Hence, the critical time step is only limited to explicit time integration. The structure of the mass matrix integrated explicitly is diagonal and this structure is known to yield smaller maximum eigenvalues [8], i.e., a greater critical time step. Furthermore, the diagonal matrices do not require a cumbersome matrix inversion. The inverse of a diagonal matrix is just the reciprocal for each entry. Because all entries are equal to 1, an inversion is no longer required.

Overall, could an IMEX time integration method increase the efficiency of the computation of lumped IGA-FCM with approximate dual basis functions. The accuracy and performance, in terms of run time, remain to be investigated.

4.2.2 Degree of polynomial reproduction for approximate dual basis functions

Within this work, the degree of polynomial reproduction q of the approximate dual basis functions was always set to its maximum, i.e., $p = q$. Lower degrees of polynomial reproduction remains to be investigated.

Appendix A

Appendix

A.1 Explicit formulas for F_ν

Explicit formulas for the computation of the homogeneous polynomial $F_\nu(x_1, \ldots, x_r)$ for $\nu = 1, \ldots, 5$ are derived from [33] [17]. The centered moment σ_l is defined by

$$\sigma_l = \frac{1}{r}\sum_{j=1}^{r}(x_j - \bar{x})^l \quad \text{with} \quad \bar{x} = \frac{1}{r}\sum_{j=1}^{r} x_j. \tag{A.1}$$

The homogeneous polynomial $F_\nu(x_1, \ldots, x_r)$ for $\nu = 1, \ldots, 5$ is given by

$$F_0(x_1, \ldots, x_r) = 1.0, \tag{A.2}$$

$$F_1(x_1, \ldots, x_r) = r^2\sigma_2, \tag{A.3}$$

$$F_2(x_1, \ldots, x_r) = \frac{1}{2}[r^2(r^2 - 3r + 3)\sigma_2^2 - r^2(r-1)\sigma_4], \tag{A.4}$$

$$\begin{aligned} F_3(x_1, \ldots, x_r) = \frac{1}{6}[&r^3(r-2)(r^2 - 7r + 15)\sigma_2^3 - 3r^3(r-2)(r^2 - 5r + 10)\sigma_4\sigma_2 - \\ &2r^2(3r^2 - 15r + 20)\sigma_3^2 + 2r^2(r-1)(r-2)\sigma_6], \end{aligned} \tag{A.5}$$

$$\begin{aligned} F_4(x_1, \ldots, x_r) = \frac{1}{24}[&r^4(r^4 - 18r^3 + 125r^2 - 384r + 441)\sigma_2^4 - \\ &6r^3(r^4 - 16r^3 + 104r^2 - 305r + 336)\sigma_4\sigma_2^2 + \\ &3r^3(r^4 - 14r^3 + 95r^2 - 322r + 420)\sigma_4^2 + \\ &8r^2(r-2)(r-3)(r^2 - 7r + 21)\sigma_6\sigma_2 - \\ &8r^3(r-3)(3r^2 - 24r + 56)\sigma_3^2\sigma_2 + \\ &48r^2(r-3)(r^2 - 7r + 14)\sigma_5\sigma_3 - \\ &6r^2(r-1)(r-2)(r-3)\sigma_8], \end{aligned} \tag{A.6}$$

$$
\begin{aligned}
F_5(x_1,\ldots,x_r) = \frac{1}{120}[&r^5(r-4)(r^4-26r^3+261r^2-1176r+2025)\sigma_2^5- \\
&10r^4(r-4)(r^4-24r^3+230r^2-999r+1674)\sigma_4\sigma_2^3+ \\
&20r^3(r-4)(r^4-20r^3+168r^2-645r+972)\sigma_6\sigma_2^2+ \\
&15r^3(r-4)(r^4-22r^3+211r^2-942r+1620)\sigma_4^2\sigma_2- \\
&20r^4(3r^4-60r^3+470r^2-1665r+2232)\sigma_3^2\sigma_2^2- \\
&30r^2(r-2)(r-3)(r-4)(r^2-9r+36)\sigma_8\sigma_2- \\
&20r^2(r^4-18r^3+173r^2-828r+1512)\sigma_6\sigma_4+ \\
&240r^3(r^4-19r^3+143r^2-493r+648)\sigma_5\sigma_3\sigma_2+ \\
&20r^4(r-4)(3r^2-30r+83)\sigma_4\sigma_3^2- \\
&24r^2(5r^4-90r^3+655r^2-2250r+3024)\sigma_5^2- \\
&240r^2(r-3)(r-4)(r^2-9r+24)\sigma_7\sigma_3+ \\
&24r^2(r-1)(r-2)(r-3)(r-4)\sigma_{10}].
\end{aligned}
\tag{A.7}
$$

Bibliography

[1] T. Hughes, J. Cottrell, and Y. Bazilevs, "Isogeometric analysis: Cad, finite elements, nurbs, exact geometry and mesh refinement," *Computer Methods in Applied Mechanics and Engineering*, vol. 194, no. 39, pp. 4135–4195, 2005, ISSN: 0045-7825. DOI: https://doi.org/10.1016/j.cma.2004.10.008. [Online]. Available: https://www.sciencedirect.com/science/article/pii/S0045782504005171.

[2] D. F. Rogers, *An introduction to NURBS: with historical perspective*. Morgan Kaufmann, 2001.

[3] V. P. Nguyen, C. Anitescu, S. P. Bordas, and T. Rabczuk, "Isogeometric analysis: An overview and computer implementation aspects," *Mathematics and Computers in Simulation*, vol. 117, pp. 89–116, 2015.

[4] Y. Bazilevs, V. M. Calo, J. A. Cottrell, *et al.*, "Isogeometric analysis using t-splines," *Computer methods in applied mechanics and engineering*, vol. 199, no. 5-8, pp. 229–263, 2010.

[5] D. C. Thomas, L. Engvall, S. K. Schmidt, K. Tew, and M. A. Scott, "U-splines: Splines over unstructured meshes," *Computer Methods in Applied Mechanics and Engineering*, vol. 401, p. 115 515, 2022.

[6] X. Li and T. W. Sederberg, "S-splines: A simple surface solution for iga and cad," *Computer Methods in Applied Mechanics and Engineering*, vol. 350, pp. 664–678, 2019.

[7] T. J. Hughes, J. A. Evans, and A. Reali, "Finite element and nurbs approximations of eigenvalue, boundary-value, and initial-value problems," *Computer Methods in Applied Mechanics and Engineering*, vol. 272, pp. 290–320, 2014.

[8] T. Bürchner, P. Kopp, S. Kollmannsberger, and E. Rank, "Isogeometric multi-resolution full waveform inversion based on the finite cell method," *Computer Methods in Applied Mechanics and Engineering*, vol. 417, p. 116 286, 2023.

[9] A. Düster, E. Rank, and B. Szabó, "The p-version of the finite element and finite cell methods," *Encyclopedia of computational mechanics second edition*, pp. 1–35, 2017.

[10] T. Bürchner, P. Kopp, S. Kollmannsberger, and E. Rank, "Immersed boundary parametrizations for full waveform inversion," *Computer Methods in Applied Mechanics and Engineering*, vol. 406, p. 115 893, 2023.

[11] A. Fichtner, *Full seismic waveform modelling and inversion*. Springer Science & Business Media, 2010.

[12] L. Guasch, O. Calderón Agudo, M.-X. Tang, P. Nachev, and M. Warner, "Full-waveform inversion imaging of the human brain," *NPJ digital medicine*, vol. 3, no. 1, p. 28, 2020.

[13] R. G. Pratt, L. Huang, N. Duric, and P. Littrup, “Sound-speed and attenuation imaging of breast tissue using waveform tomography of transmission ultrasound data,” in *Medical Imaging 2007: Physics of Medical Imaging*, SPIE, vol. 6510, 2007, pp. 1523–1534.

[14] J. Rao, M. Ratassepp, and Z. Fan, “Investigation of the reconstruction accuracy of guided wave tomography using full waveform inversion,” *Journal of Sound and Vibration*, vol. 400, pp. 317–328, 2017.

[15] R. Seidl, “Full waveform inversion for ultrasonic nondestructive testing,” Ph.D. dissertation, Technische Universität München, 2018.

[16] C. Faßbender, T. Bürchner, P. Kopp, E. Rank, and S. Kollmannsberger, “Implicit-explicit time integration for the immersed wave equation,” *Computers & Mathematics with Applications*, vol. 163, pp. 1–13, 2024.

[17] T.-H. Nguyen, R. R. Hiemstra, S. Eisenträger, and D. Schillinger, “Towards higher-order accurate mass lumping in explicit isogeometric analysis for structural dynamics,” *Computer Methods in Applied Mechanics and Engineering*, vol. 417, p. 116 233, 2023.

[18] R. Hiemstra, T.-H. Nguyen, S. Eisentrager, W. Dornisch, and D. Schillinger, “Higher order accurate mass lumping for explicit isogeometric methods based on approximate dual basis functions,” *arXiv preprint arXiv:2310.13379*, 2023.

[19] W. Dornisch, J. Stöckler, and R. Müller, “Dual and approximate dual basis functions for b-splines and nurbs – comparison and application for an efficient coupling of patches with the isogeometric mortar method,” *Computer Methods in Applied Mechanics and Engineering*, vol. 316, pp. 449–496, 2017, Special Issue on Isogeometric Analysis: Progress and Challenges, ISSN: 0045-7825. DOI: https://doi.org/10.1016/j.cma.2016.07.038. [Online]. Available: https://www.sciencedirect.com/science/article/pii/S0045782516308209.

[20] S. Held, S. Eisenträger, and W. Dornisch, “An efficient mass lumping scheme for isogeometric analysis based on approximate dual basis functions,” *arXiv preprint arXiv:2306.12257*, 2023.

[21] C. Anitescu, C. Nguyen, T. Rabczuk, and X. Zhuang, “Isogeometric analysis for explicit elastodynamics using a dual-basis diagonal mass formulation,” *Computer Methods in Applied Mechanics and Engineering*, vol. 346, pp. 574–591, 2019.

[22] H. Igel, *Computational seismology: a practical introduction*. Oxford University Press, 2017.

[23] C. De Boor and C. De Boor, *A practical guide to splines*. springer-verlag New York, 1978, vol. 27.

[24] T. J. Hughes, *The finite element method: linear static and dynamic finite element analysis*. Courier Corporation, 2012.

[25] M. Kelemen, “A review of mass lumping schemes for the spectral cell method,” 2021.

[26] C. Faßbender, “Time integration for the spectral cell method with application to the full waveform inversion,” 2023.

[27] C. de Boor, *On local linear functionals which vanish at all b-splines but one, theory of approximation (conference proc., calgary, 1975, ed. ag law and bn sahney)*, 1976.

[28] L. Schumaker, *Spline functions: basic theory*. Cambridge university press, 2007.

[29] P. Oswald and B. Wohlmuth, "On polynomial reproduction of dual fe bases," in *Thirteenth international conference on domain decomposition methods*, 2001, pp. 85–96.

[30] C. L. Lawson and R. J. Hanson, *Solving least squares problems*. SIAM, 1995.

[31] W. Dornisch, G. Vitucci, and S. Klinkel, "The weak substitution method–an application of the mortar method for patch coupling in nurbs-based isogeometric analysis," *International Journal for Numerical Methods in Engineering*, vol. 103, no. 3, pp. 205–234, 2015.

[32] W. Dornisch, G. Vitucci, and S. Klinkel, "The weak substitution method – an application of the mortar method for patch coupling in nurbs-based isogeometric analysis," *International Journal for Numerical Methods in Engineering*, vol. 103, no. 3, pp. 205–234, 2015. DOI: https://doi.org/10.1002/nme.4918. eprint: https://onlinelibrary.wiley.com/doi/pdf/10.1002/nme.4918. [Online]. Available: https://onlinelibrary.wiley.com/doi/abs/10.1002/nme.4918.

[33] C. K. Chui, W. He, and J. Stöckler, "Nonstationary tight wavelet frames, i: Bounded intervals," *Applied and Computational Harmonic Analysis*, vol. 17, no. 2, pp. 141–197, 2004, Special Issue: Frames in Harmonic Analysis, Part II, ISSN: 1063-5203. DOI: https://doi.org/10.1016/j.acha.2004.02.004. [Online]. Available: https://www.sciencedirect.com/science/article/pii/S1063520304000454.

[34] E. Rank, M. Ruess, S. Kollmannsberger, D. Schillinger, and A. Düster, "Geometric modeling, isogeometric analysis and the finite cell method," *Computer Methods in Applied Mechanics and Engineering*, vol. 249, pp. 104–115, 2012.

[35] N. Zander, T. Bog, S. Kollmannsberger, D. Schillinger, and E. Rank, "Multi-level hp-adaptivity: High-order mesh adaptivity without the difficulties of constraining hanging nodes," *Computational Mechanics*, vol. 55, no. 3, pp. 499–517, 2015.

[36] M. Géradin and D. J. Rixen, *Mechanical vibrations: theory and application to structural dynamics*. John Wiley & Sons, 2014.

[37] J. Parvizian, A. Düster, and E. Rank, "Finite cell method: H-and p-extension for embedded domain problems in solid mechanics," *Computational Mechanics*, vol. 41, no. 1, pp. 121–133, 2007.

[38] S. Hubrich, P. Di Stolfo, L. Kudela, *et al.*, "Numerical integration of discontinuous functions: Moment fitting and smart octree," *Computational Mechanics*, vol. 60, pp. 863–881, 2017.

[39] Y. Voet, E. Sande, and A. Buffa, "A mathematical theory for mass lumping and its generalization with applications to isogeometric analysis," *Computer Methods in Applied Mechanics and Engineering*, vol. 410, p. 116 033, 2023.

[40] J. A. Cottrell, A. Reali, Y. Bazilevs, and T. J. Hughes, “Isogeometric analysis of structural vibrations,” *Computer methods in applied mechanics and engineering*, vol. 195, no. 41-43, pp. 5257–5296, 2006.

[41] M. Meßmer, T. Teschemacher, L. F. Leidinger, R. Wüchner, and K.-U. Bletzinger, “Efficient cad-integrated isogeometric analysis of trimmed solids,” *Computer Methods in Applied Mechanics and Engineering*, vol. 400, p. 115 584, 2022.

[42] L. Leidinger, “Explicit isogeometric b-rep analysis for nonlinear dynamic crash simulations: Integrating design and analysis by means of trimmed multi-patch shell structures,” Ph.D. dissertation, Technische Universität München, 2020.

[43] L. Radtke, M. Torre, T. J.R. Hughes, D. Alexander, S. Giancarlo, and R. Alessandro, “An analysis of high oder FEM and IGA for explicit dynamics: Mass lumping and immersed boundary,” *International Journal for Numerical Methods in Engineering*, Accepted for Publication 2024.

Declaration

I hereby affirm that I have independently written the thesis submitted by me and have not used any sources or aids other than those indicated.

Location, Date, Signature